Constitutive model for swelling properties of unsaturated bentonite buffer materials during saturation

Ito, Shinji
Tachibana, Shinya
Takeyama, Tomohide
Iizuka, Atsushi

(Citation)
Soils and Foundations,62(4):101161

(Issue Date)
2022-08

(Resource Type)
journal article

(Version)
Version of Record

HOSTED BY

ELSEVIER

Available online at www.sciencedirect.com

ScienceDirect

Soils and Foundations 62 (2022) 101161

www.elsevier.com/locate/sandf

Technical Paper

Constitutive model for swelling properties of unsaturated bentonite buffer materials during saturation

Shinji Ito [a], Shinya Tachibana [b,*], Tomohide Takeyama [c], Atsushi Iizuka [b]

[a] *Civil Engineering Design Division, Kajima Corporation, Japan*
[b] *Research Center for Urban Safety and Security, Kobe University, Japan*
[c] *Department of Civil Engineering, Graduate School of Engineering, Kobe University, Japan*

Received 3 June 2021; received in revised form 21 March 2022; accepted 10 April 2022

Abstract

Bentonite-based materials are candidate buffer materials for the geological disposal of radioactive waste in many countries. Once the disposal facility is closed and the groundwater level recovers, the buffer will gradually become saturated by the infiltration of groundwater. The swelling properties of saturated bentonite affect the distribution of dry density and the stress state within the buffer. Therefore, to evaluate the long-term safety of the buffer, a model must be developed that can continuously express the mechanical behavior of bentonite from the construction and operation of the repository for disposal (the unsaturated state) to the resaturation phase (saturated state). In this study, the existing elastoplastic constitutive model for saturated expansive soils was extended to predict the mechanical response in the unsaturated state. In formulating this model, the effective degree of saturation and the plastic volumetric strain were employed as the hardening parameters to express the changes in stiffness and swelling properties due to desaturation or saturation. In addition, a method was proposed for estimating the material parameters added to the expanded constitutive model. This study demonstrated the validity of the proposed constitutive model and the parameter estimation method by comparing the results of simulations with those of laboratory tests.

Keywords: Elastoplastic constitutive equation; Expansive soils; Bentonite; Swelling; Unsaturated soils

1. Introduction

In a geological repository system for the disposal of high-level radioactive waste, compacted bentonite or bentonite–sand mixtures are used as buffer and backfilling materials. These materials are expected to provide low hydraulic permeability and self-sealing properties owing to their high swelling potential and high radionuclide retardation capacities (Pusch, 1979; Yong et al., 1986; Villar and Lloret, 2008; Komine and Watanabe, 2010). After the closure of the repository, groundwater from the surrounding host rock gradually penetrates the buffer, which is initially unsaturated during the construction and operation of the repository. The buffer swells on exposure to groundwater, and subsequently, seals the gaps that formed during construction, such as those between the buffer and the waste canister or the surrounding host rock. As the volumetric swelling deformation of the buffer is confined, swelling pressure is generated with further groundwater infiltration; this changes the stress and dry density distributions within the buffer.

Since the buffer is a crucial component of all repositories, it is necessary to develop a mathematical model that continuously expresses the mechanical behavior of the buf-

Peer review under responsibility of The Japanese Geotechnical Society.
* Corresponding author.
E-mail address: stachi@people.kobe-u.ac.jp (S. Tachibana).

https://doi.org/10.1016/j.sandf.2022.101161
0038-0806/

fer during its transition from an unsaturated state to a saturated state in order to design repositories and evaluate their long-term safety. Various models have been developed to express the swelling behavior of expansive soils including bentonite. Some researchers have proposed methods based on the diffuse double-layer theory to determine the reaction and repulsion forces generated between crystal layers owing to the physiochemical effects. These methods have reproduced the swelling pressure obtained through laboratory tests conducted on compacted bentonite (Komine and Ogata, 1996; Tripathy, 2004; Schanz, 2013). Meanwhile, many studies have investigated constitutive modeling based on the elastoplastic theory. Before applying these constitutive models to expansive soils, several constitutive models were proposed to describe the mechanical responses of unsaturated soil, such as volumetric contraction upon drying and collapse behavior due to saturation (Alonso et al., 1990; Kohgo et al., 1993, Karube and Kawai, 2001). However, these constitutive models were developed for non-expansive soils. Therefore, approaches have also been proposed that combine the above-described pioneering constitutive model framework and new concepts to express the unique properties of expansive soils. One novel method divides the pore structures of expansive soils into macropores formed by the soil particle skeleton and micropores existing in the crystal layers (Alonso and Gens, 1999; Sánchez et al., 2005; Mašin, 2013). Mercury intrusion tests have verified that expansive soils have two types of pore structures (Sánchez et al., 2005; Romero and Simms, 2008; Seiphoori et al., 2014). The important equations in the constitutive model for the concept of this double structure are (i) the stress–strain relation of the macrostructure, (ii) the stress–strain relation of the microstructure, and (iii) the coupling function describing the interaction between the two structures. In the model proposed by Alonso and Gens (1999), the elastoplastic constitutive model for unsaturated non-expansive soils was used for (i). The deformation arising from the microstructure was assumed to be elastic and volumetric; therefore, the relation between the effective mean stress and volumetric microstructural strain was used for (ii). The effective mean stress was described by the effective stress equation proposed by Bishop (1959), which considered the decrease in effective mean stress caused by the loss of suction under constant confining stress. Therefore, as the effective mean stress decreased during the process of attaining saturation, swelling deformation occurred in the microstructure. As the total volume change is the sum of the changes in the macrostructure and the changes in the microstructure, the total swelling deformation comprises the deformation in the microstructure, and a large swelling deformation can be expressed. Furthermore, the coupling function (iii) was defined such that the elastic deformation in the microstructure, due to the change in suction, contributed to the occurrence of plastic deformation in the macrostructure. Mašin (2013) also developed a constitutive model based on the concept of a double structure. The hypoplastic model for unsaturated soils was applied for (i), and a concept similar to that of Gens and Alonso (1999) was used for (ii). A coupling function was proposed to describe the effect of the macropore closure under the microstructural swelling deformation caused by the decrease in suction. A constitutive model including the concept of the double structure is advantageous because the existing constitutive model for non-expansive soils can be directly applied to the stress–strain relation in the macrostructure.

Other studies have proposed constitutive models that macroscopically and phenomenologically express the mechanical responses observed in laboratory tests (Sun and Sun, 2012; Li and Yang, 2017; Takayama et al., 2017). Sun and Sun (2012) proposed the concept of the equivalent void ratio curve and incorporated it into a constitutive model for unsaturated non-expansive soils. Li and Yang (2017) developed a constitutive model with the concept of a macrostructural neutral loading line. The idea of linking these two models involves the treatment of the large swelling deformation of expansive soils as plastic deformation. In contrast, Takayama et al. (2017) regarded the swelling behavior of expansive soils as an elastic response and proposed a model considering the dependency of the elastic bulk modulus on the degree of saturation. As described above, the swelling behavior of expansive soils can be interpreted as either plastic deformation or elastic deformation in macroscopic approaches.

Tachibana et al. (2020) also developed a constitutive model that macroscopically and phenomenologically expresses the mechanical responses of expansive soils in the saturated state. They achieved this by introducing the plastic rebound concept (Amerashinghe and Kraft, 1983) to the modified Cam–Clay model (Roscoe and Burland, 1968). The simulated results confirmed that this model can sufficiently reproduce the stress paths in the consolidation and swelling processes as well as large swelling upon unloading. Furthermore, for the simplicity of the model, only one new parameter was added to the base parameters of the modified Cam–Clay model.

To provide a more comprehensive understanding of the mechanical, hydraulic, thermal, and chemical behavior in the near-field of a repository, constitutive models considering the thermal and chemical effects, in addition to the hydraulic effects (e.g., Dupray et al., 2013; Sánchez et al., 2016), and models reflecting the chemical effects (e.g., Guimarães et al., 2013; Kyokawa et al., 2020) have been proposed. Although developing a constitutive model incorporating the thermal and chemical effects is important for designing repositories and evaluating their long-term safety, this study focuses on the interaction between the mechanical and hydraulic behavior of the buffer material. Additionally, the elastoplastic constitutive model by Tachibana et al. (2020) is extended to describe the mechanical response of unsaturated expansive soils, especially the swelling property under saturation.

In this study, the framework of the elastoplastic constitutive model for unsaturated soils is employed to extend the constitutive model. Sheng (2011) reported that there were three approaches (A: Separate stress and suction approach; B: Combined stress–suction approach; and C: Sheng-Fredlund-Gens (SFG) approach, which is a middle ground between A and B) to describe the mechanical behavior of unsaturated soils, especially focusing on the volume change. In this study, the constitutive model is formulated by applying the framework of the elasto-plastic constitutive model for unsaturated soils proposed by Ohno et al. (2007), which is classified as Approach B. A method for estimating newly added parameters is also proposed. Furthermore, this study examines the validity of the proposed constitutive model and the parameter estimation method by comparing the results of simulations and laboratory tests.

2. Constitutive modeling

2.1. Elastoplastic constitutive model with plastic rebound concept

Tachibana et al. (2020) developed an elastoplastic constitutive model for expansive soils in the saturated state that was based on the modified Cam–Clay model. As shown in Fig. 1, the plastic rebound line (PRL) is newly defined in this model, and the elastic domain is bounded by both the normally consolidated line (NCL) and the PRL. With the elliptical yield surface, the yield function is expressed as follows:

$$f(p', q, p'_c, p'_s) = \frac{q^2}{\tilde{M}^2} + (p' - p'_c)(p' - p'_s) = 0 \tag{1}$$

where $\tilde{M}$ is the material constant specifying the elliptical ratio of the yield surface. p' and q are the effective mean stress and stress deviator, respectively, defined as.

$$p' = \mathrm{tr}\boldsymbol{\sigma}'/3,\ q = \sqrt{3/2}||\boldsymbol{s}||,\ \boldsymbol{s} = \boldsymbol{\sigma}' - p'\boldsymbol{I} \tag{2}$$

where $\boldsymbol{\sigma}'$ is the effective stress tensor, $\boldsymbol{s}$ is the deviatoric stress tensor, and $\boldsymbol{I}$ is the second-order identity tensor. p'_c and p'_s are the yield stresses under isotropic loading and unloading, respectively. Yield stresses p'_c and p'_s always satisfy the following relation:

$$\frac{p'_s}{p'_c} = \frac{\zeta}{1+\zeta} \tag{3}$$

where ζ is the material constant specifying the space between the NCL and the PRL. Critical state parameter M can be written as.

$$M = \frac{\tilde{M}}{1+2\zeta} \tag{4}$$

Yield stresses p'_c and p'_s are expressed by plastic volumetric strain ε_v^p, as follows:

$$\frac{p'_c}{p'_{c0}} = \frac{p'_s}{p'_{s0}} = \exp\left(\frac{1+e_{c0}}{\lambda-\kappa}\varepsilon_v^p\right) \tag{5}$$

where p'_{c0},p'_{s0}, and e_{c0} are p'_c,p'_c, and a reference void ratio at the onset of plastic volumetric strain, respectively. λ is the compression index and κ is the swelling index. Assuming the associated flow rule ($\dot{\varepsilon}_v^p = \gamma\partial f/\partial p'; \gamma > 0$) to define plastic volumetric strain rate $\dot{\varepsilon}_v^p$, when p'_c and p'_s decrease, the yield surface shrinks on the left side of the yield surface ($\partial f/\partial p' < 0$), as shown in Fig. 1. In contrast, when p'_c and p'_s increase, the yield surface expands on the right side of the yield surface ($\partial f/\partial p' > 0$). In addition, the rate of p'_c and p'_s can be written with plastic volumetric strain rate $\dot{\varepsilon}_v^p$, as follows:

$$\frac{\dot{p}'_c}{p'_c} = \frac{\dot{p}'_s}{p'_s} = \frac{1+e_{c0}}{\lambda-\kappa}\dot{\varepsilon}_v^p \tag{6}$$

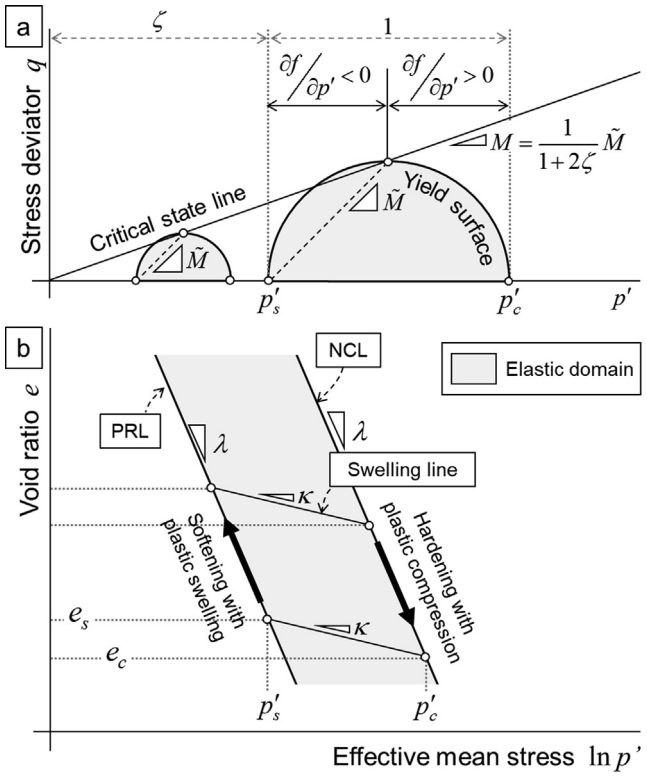

Fig. 1. Conceptual schematics of (a) yield surface in $q - p'$ space and (b) NCL, PRL, and swelling line in $e - \ln p'$ space of elasto-plastic constitutive model with concept of plastic rebound.

2.2. S_e-hardening model

The S_e-hardening model employs the effective degree of saturation in addition to the plastic volumetric strain as the hardening parameter, which contributes to the expansion and contraction of the yield surface. This model can express the increase in stiffness due to desaturation and the collapse behavior due to the decrease in suction. It is based on Bishop's effective stress for unsaturated soils,

for which the effective degree of saturation is employed as Bishop's parameter, as follows:

$$\boldsymbol{\sigma}' = \boldsymbol{\sigma}^{net} + p_{suc}\mathbf{1};\ \boldsymbol{\sigma}^{net} = \boldsymbol{\sigma} - p_a\mathbf{1},\ p_{suc} = sS_e \tag{7}$$

where $\boldsymbol{\sigma}^{net}$ is the net stress tensor, p_{suc} is the suction stress, $\boldsymbol{\sigma}$ is the total stress tensor, s is the suction, and S_e is the effective degree of saturation. Suction s and effective degree of saturation S_e are defined by.

$$s = p_a - p_w,\ S_e = (S_r - S_{r0})/(1 - S_{r0}) \tag{8}$$

where p_a is the pore air pressure, p_w is the pore water pressure, S_r is the degree of saturation, and S_{r0} is the degree of saturation as $s \to \infty$. Fig. 2 shows conceptual schematics of the relationship among effective mean stress p', stress deviator q, and void ratio e in this model. The model assumes that the normal compression lines of the constant effective degree of saturation are parallel to each other in the $e - \ln p'$ space. Yield stress p'_c is given as the product of variable ξ and reference yield stress $\bar{p}'_c$, which is a function of plastic volumetric strain ε_v^p, as follows:

$$p'_c = \xi(S_e) \cdot \bar{p}'_c\left(\varepsilon_v^p\right) \tag{9}$$

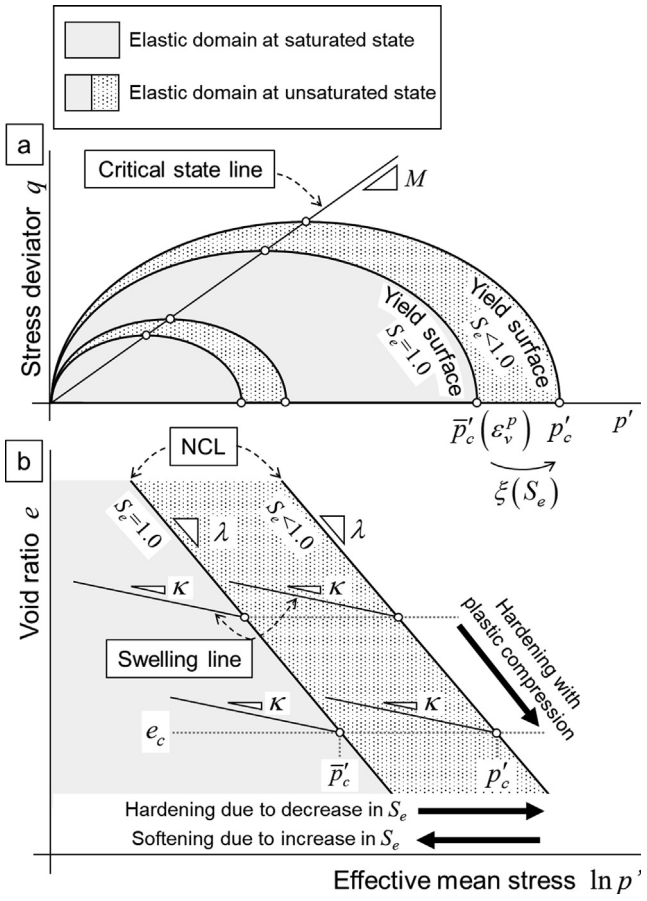

Fig. 2. Conceptual schematics of (a) yield surfaces in $q - p'$ space and (b) NCL and swelling line in $e - \ln p'$ space of S_e-hardening model.

where variable ξ is a function of effective degree of saturation S_e and determines the effect of unsaturation on the yield stress. Variable ξ is given as.

$$\xi = \exp\left[(1 - S_e)^n \ln a\right] \tag{10}$$

where a and n are material constants. As shown in Fig. 2, yield stress p'_c and reference yield stress $\bar{p}'_c$ have the same void ratio e_c in the $e - \ln p'$ space. In the elastic state, yield stress p'_c increases or decreases with changes in the effective degree of saturation at a constant void ratio e_c at yield, whereas reference yield stress $\bar{p}'_c$ remains unchanged because no plastic deformation occurs. In other words, reference yield stress $\bar{p}'_c$ and void ratio e_c at yield can change owing to the development of the plastic volumetric strain. Assuming an elliptical yield surface, the yield function can be written as.

$$f\left(p', q, p'_c\right) = \frac{q^2}{M^2} + p'\left(p' - p'_c\right) = 0 \tag{11}$$

As observed in Fig. 2, Eq. (11) indicates that the yield surface similarly expands or contracts with changes in the effective degree of saturation.

2.3. Concept of proposed constitutive model

The framework of the S_e-hardening model is incorporated in the elastoplastic constitutive model with the concept of plastic rebound. Takayama et al. (2018) reported that the effective degree of saturation was appropriate as a hardening parameter for bentonite materials by using one-dimensional compression lines for the constant degree of saturation of Kunigel V1 (sodium-type bentonite) obtained by Kobayashi et al. (2007). Hence, in this study, a model is considered in which the PRL as well as the NCL moves in the $e - \ln p'$ space as the effective degree of saturation increases or decreases, so that the elastic region in the drier unsaturated state encompasses the elastic region in the wetter state, as shown in Fig. 3. This conceptual modeling makes it possible to represent the isotropic responses of the saturation process, as shown in Fig. 4. The figure shows two paths of saturation starting from point I, which is unsaturated and located on the PRL. One path leads to point S1, under the constant net mean stress condition, and the other path leads to point S2, under the constant volume or constant void ratio condition. In both cases, it is assumed that there is an equivalent decrease in suction stress in the process of reaching the saturation state ($\Delta p_{suc} < 0$). The path leading to point S1 is accompanied by plastic swelling as it continues to intersect the PRL moving to the right, while the suction stress and effective mean stress decrease equivalently ($\Delta p'_1 = \Delta p_{suc} < 0$). The path leading to point S2, on the other hand, represents the increase in mean effective stress as the PRL moves to the right. This increase in mean effective stress and decrease in suction stress allow for an increase in net stress, i.e., the development of swelling pres-

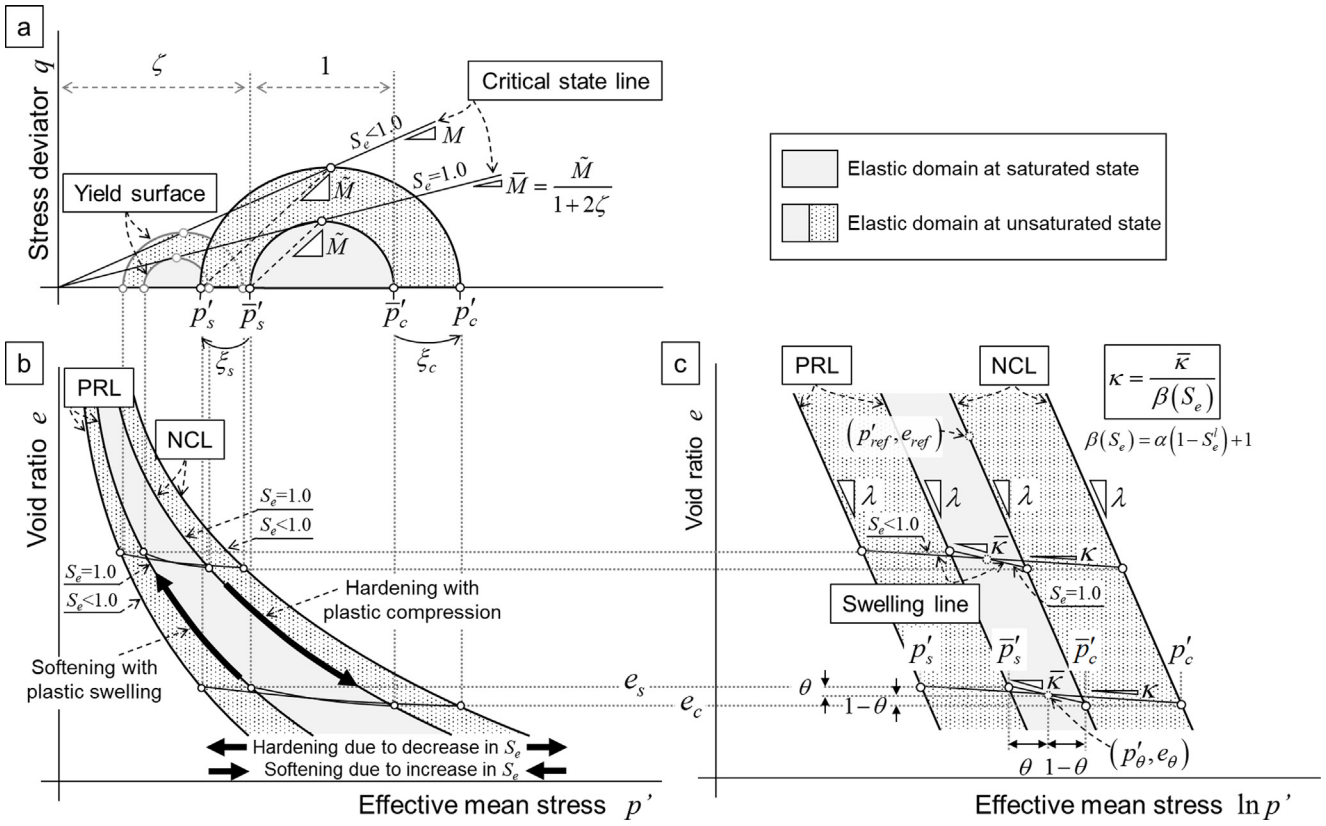

Fig. 3. Conceptual schematics of (a) yield surfaces in $q - p'$ space, (b) NCL, PRL, and swelling line in $e - p'$ space, and (c) NCL, PRL, and swelling line in $e - \ln p'$ space of proposed constitutive model.

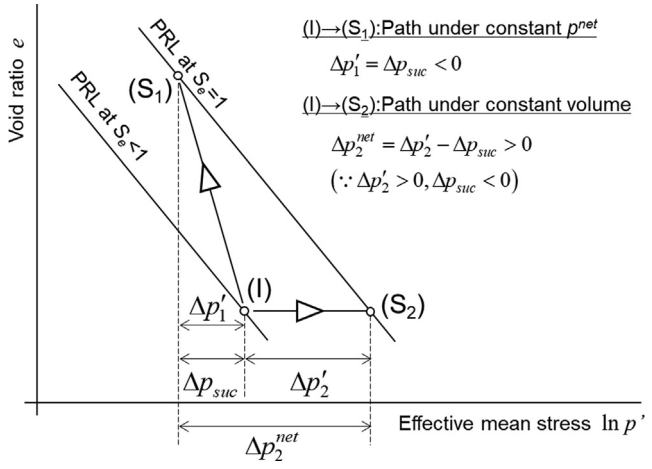

Fig. 4. Conceptual schematic of responses in $e - \ln p'$ due to movement of PRL during saturation.

sure due to saturation ($\Delta p_2^{net} = \Delta p_2' - \Delta p_{suc} > 0$). As with the S_e-hardening model, plastic volumetric strain ε_v^p and effective degree of saturation S_e are employed as the hardening parameters to describe yield stresses p_c' and p_s' as the following equations:

$$p_c' = \xi_c(S_e) \cdot \bar{p}'_c\left(\varepsilon_v^p\right) \tag{12}$$

$$p_s' = \xi_s(S_e) \cdot \bar{p}'_s\left(\varepsilon_v^p\right) \tag{13}$$

where ξ_c and ξ_s are the functions of the effective degree of saturation used to determine the effect of unsaturation on the NCL and PRL, respectively. $\bar{p}'_c$ and $\bar{p}'_s$ are the reference yield stresses, which are functions of the plastic volumetric strain. Instead of Eq. (3), reference yield stresses $\bar{p}'_c$ and $\bar{p}'_s$ satisfy the following relation:

$$\frac{\bar{p}'_s}{\bar{p}'_c} = \frac{\zeta}{1+\zeta} \tag{14}$$

Yield stress p_c' and reference yield stress $\bar{p}'_c$ have the same void ratio e_c at yield in the $e - \ln p'$ space. Similarly, p_s' and $\bar{p}'_s$ have the same void ratio e_s at yield.

An illustration of the hardening/softening is given in Fig. 5. Yield stresses p_c' and p_s' can change due to the contribution of effective degree of saturation S_e even if the state is elastic. Therefore, variables ξ_c and ξ_s are assumed to be functions of effective degree of saturation S_e only and not dependent on plastic volumetric strain ε_v^p. In other words, functions ξ_c and ξ_s cannot be formulated separately as functions of the degree of saturation, but must be formulated under constraints that do not lead to changes in the void ratios at yield, namely, e_c and e_s.

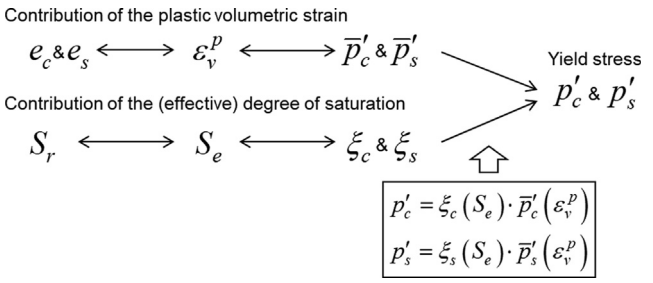

Fig. 5. Contributions of plastic volumetric strain ε_v^p and effective degree of saturation S_e to hardening/softening.

Fig. 6 shows the path from point I (initial state) to point A (current state) with a change in the effective degree of saturation in the elastic state. Points I and A are located between the NCL and PRL corresponding to the initial and current states, respectively. As explained above, the void ratios at yield, e_c and e_s, must not change from their initial values in order to avoid the development of plastic volumetric strain in the elastic state. Therefore, if the swelling line is assumed to be a straight line, passing through (p'_c, e_c) and (p'_s, e_s) in the $e - \ln p'$ space, swelling index κ, which is the gradient of the line, should be a function of the degree of saturation. Yamamoto et al. (2019) observed a similar tendency of the swelling index in one-dimensional compression and swelling tests on the Kunigel V1–sand mixture under constant suction conditions. The experimental results showed that the swelling index increased with decreasing suction. Thus, swelling index κ can be formulated as.

$$\kappa = \frac{\bar{\kappa}}{\beta(S_e)} \tag{15}$$

where $\bar{\kappa}$ is the swelling index at the saturated state and β is a function of the effective degree of saturation S_e. It should be noted that β is a monotonic decreasing function that satisfies the expression $\beta(1) = 1$. In this study, variable β is given by.

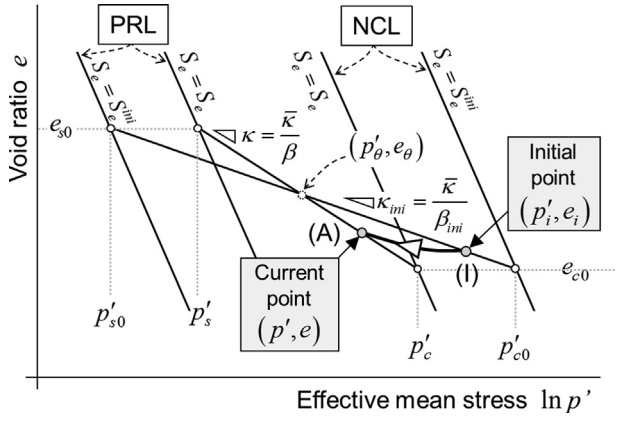

Fig. 6. Conceptual schematic of elastic response in $e - \ln p'$ space with increase in effective degree of saturation.

$$\beta(S_e) = \alpha\left(1 - S_e^l\right) + 1 \tag{16}$$

where α and l are the material constants within the range of $\alpha > 0$ and $l > 0$.

In addition to the above formulation for the slope of the swelling line, the position of the swelling line must be determined in order to specify the yield surface at any given degree of saturation. In this study, it is assumed that the swelling line at any given degree of saturation always passes through a point $(p', e) = (p'_\theta, e_\theta)$, as shown in Fig. 3. It should be noted that p'_θ is the stress that internally divides $\bar{p}'_c$ and $\bar{p}'_s$ by $\theta : 1 - \theta$, e_θ is the void ratio that internally divides e_c and e_s by $\theta : 1 - \theta$, and θ is the material constant within the range of $0 < \theta < 1$. In other words, the changes in p'_θ and e_θ occur only because of the development of plastic volumetric strain. The relations between p'_θ and $\bar{p}'_c$ and between p'_θ and $\bar{p}'_s$ can be written, respectively, as

$$p'_\theta = \frac{\theta + \zeta}{1 + \zeta}\bar{p}'_c \tag{17}$$

and

$$p'_\theta = \frac{\theta + \zeta}{\zeta}\bar{p}'_s \tag{18}$$

Then, the swelling lines at the unsaturated state passing through $(p'_c, e_c), (p'_\theta, e_\theta)$, and (p'_s, e_s) can be formulated as

$$e_\theta - e_c = \kappa \ln\left(p'_c / p'_\theta\right) \tag{19}$$

$$e_\theta - e_s = \kappa \ln\left(p'_s / p'_\theta\right) \tag{20}$$

On the other hand, the swelling lines at the saturated state passing through $\left(\bar{p}'_c, e_c\right), (p'_\theta, e_\theta)$, and $\left(\bar{p}'_s, e_s\right)$ can be formulated as

$$e_\theta - e_c = \bar{\kappa} \ln\left(\bar{p}'_c / p'_\theta\right) \tag{21}$$

$$e_\theta - e_s = \bar{\kappa} \ln\left(\bar{p}'_s / p'_\theta\right) \tag{22}$$

The elimination of $e_\theta - e_c$ between Eqs. (19) and (21) results in the following relation:

$$\kappa \ln\left(p'_c / p'_\theta\right) = \bar{\kappa} \ln\left(\bar{p}'_c / p'_\theta\right) \tag{23}$$

By substituting Eqs. (15) and (17) into Eq. (23), function ξ_c can be derived as follows:

$$\xi_c = \frac{p'_c}{\bar{p}'_c} = \exp\left[(\beta - 1)\ln\frac{1 + \zeta}{\theta + \zeta}\right] \tag{24}$$

Similarly, the elimination of $e_\theta - e_s$ between Eqs. (20) and (22) results in the following relation:

$$\kappa \ln\left(p'_s / p'_\theta\right) = \bar{\kappa} \ln\left(\bar{p}'_s / p'_\theta\right) \tag{25}$$

By substituting Eqs. (15) and (18) into Eq. (25), function ξ_s can be derived as follows:

$$\xi_s = \frac{p'_s}{\bar{p}'_s} = \exp\left[(\beta - 1)\ln\frac{\zeta}{\theta + \zeta}\right] \tag{26}$$

Variables ξ_c and ξ_s both change in conjunction with variable β. By substituting Eq. (16) into Eqs. (24) and (26), ξ_c and ξ_s can be also expressed as

$$\xi_c = \exp\left[\left(1 - S_e^l\right)\ln\left(\frac{1+\zeta}{\theta+\zeta}\right)^{\alpha}\right] \tag{27}$$

and

$$\xi_s = \exp\left[\left(1 - S_e^l\right)\ln\left(\frac{\zeta}{\theta+\zeta}\right)^{\alpha}\right]. \tag{28}$$

Assuming that the yield surface maintains the same shape at any degree of saturation, the yield function can be written as in Eq. (1), as follows:

$$f\left(p', q, p'_c, p'_s\right) = \frac{q^2}{\tilde{M}^2} + \left(p' - p'_c\right)\left(p' - p'_s\right) = 0. \tag{29}$$

According to the geometric relationship between the yield surface and the critical state line in the $q - p'$ space, shown in Fig. 3(a), critical state parameter M is given by.

$$M = \frac{\xi_c \bar{p}'_c - \xi_s \bar{p}'_s}{\xi_c \bar{p}'_c + \xi_s \bar{p}'_s}\tilde{M}. \tag{30}$$

By substituting Eqs. (14), (24), and (26) into Eq. (30), critical state parameter M can be derived as.

$$M = \frac{(1+\zeta)^{\beta} - \zeta^{\beta}}{(1+\zeta)^{\beta} + \zeta^{\beta}}\tilde{M}. \tag{31}$$

Fig. 7 shows the dependency of the effective degree of saturation S_e on variable β, swelling index κ, and critical state parameter M with material inputs of $\zeta = 0.5, \bar{M} = 1.0, \bar{\kappa} = 0.015, \alpha = 3.0$, and $l = 0.5, 1.0, 2.0$. Variable β decreases monotonically with an increase in the degree of saturation, and its maximum value is determined by parameter α ($\beta = 1 + \alpha$ at $S_e = 0$). Swelling index κ and critical state parameter M are also functions of the degree of saturation with variable β as a mediator.

Fig. 8 shows the variations in ξ_c and ξ_s with effective degree of saturation S_e. ξ_c and ξ_s are monotonic increasing and decreasing functions, respectively, that satisfy $\xi_c = 1$ and $\xi_s = 1$ at the saturated state. Parameters α and θ specify the values of ξ_c and ξ_s at $S_e = 0$, and parameter l controls the rates of change in ξ_c and ξ_s with respect to effective degree of saturation S_e.

2.4. Stress–strain relation

As shown in Fig. 6, the void ratios at point I (initial state) and point A (current state) are given by

$$e_i = e_\theta - \frac{\bar{\kappa}}{\bar{\beta}_i}\ln\frac{p'_i}{p'_\theta} \tag{32}$$

and

$$e = e_\theta - \frac{\bar{\kappa}}{\bar{\beta}}\ln\frac{p'}{p'_\theta}. \tag{33}$$

A change in the void ratio from point I to point A can be expressed as

$$e - e_i = -\frac{\bar{\kappa}}{\bar{\beta}}\ln\frac{p'}{p'_\theta} + \frac{\bar{\kappa}}{\bar{\beta}_i}\ln\frac{p'_i}{p'_\theta}. \tag{34}$$

Elastic volumetric strain ε_v^e and its rate can be written, respectively, as

$$\varepsilon_v^e = \frac{-(e - e_i)}{1 + e_{c0}} = \frac{1}{1 + e_{c0}}\left(\frac{\bar{\kappa}}{\bar{\beta}}\ln\frac{p'}{p'_\theta} - \frac{\bar{\kappa}}{\bar{\beta}_i}\ln\frac{p'_i}{p'_\theta}\right) \tag{35}$$

and

$$\dot{\varepsilon}_v^e = \frac{\kappa}{1 + e_{c0}}\frac{\dot{p}'}{p'} + \left(-\frac{1}{1 + e_{c0}}\frac{\kappa}{\beta}\frac{\partial\beta}{\partial S_e}\ln\frac{p'}{p'_\theta}\right)\dot{S}_e. \tag{36}$$

Eq. (36) provides the following equations:

$$\dot{p}' = K\dot{\varepsilon}_v^e - K_{S_e}\dot{S}_e \tag{37}$$

$$K = \frac{1 + e_{c0}}{\kappa}p', \quad K^{S_e} = -\frac{1}{\beta}\frac{\partial\beta}{\partial S_e}p'\ln\frac{(1+\zeta)p'}{(\theta+\zeta)\bar{p}'_c} \tag{38}$$

where K is the bulk modulus. By assuming Hooke's law, the relation among the rates for effective stress, elastic strain, and effective degree of saturation is given as

$$\dot{\boldsymbol{\sigma}}' = \boldsymbol{D}^e : \dot{\varepsilon}^e - K_{S_e}\dot{S}_e\boldsymbol{I} \tag{39}$$

$$\boldsymbol{D}^e = \left(K - \frac{2}{3}G\right)\boldsymbol{I}\otimes\boldsymbol{I} + 2G\boldsymbol{I}, \; G = \frac{3(1-2\nu')}{2(1+\nu')}K \tag{40}$$

where $\boldsymbol{D}^e$ is the elastic stiffness tensor, G is the shear modulus, and ν' is the effective Poisson's ratio.

The governing equations that are necessary to formulate the elastoplastic constitutive equation are as follows:

1) Yield functions (see Eq. (29)).

2) Associated flow rule: The plastic strain rate is defined by the associated flow rule.

$$\dot{\boldsymbol{\varepsilon}}^p = \gamma\frac{\partial f}{\partial\boldsymbol{\sigma}'}; \gamma > 0 \tag{41}$$

where γ is the plastic multiplier.

3) Elastic and plastic strain decomposition: It is assumed that total strain rate $\dot{\boldsymbol{\varepsilon}}$ can be decomposed into the elastic part,$\dot{\boldsymbol{\varepsilon}}^e$, and the plastic part,$\dot{\boldsymbol{\varepsilon}}^p$.

$$\dot{\boldsymbol{\varepsilon}} = \dot{\boldsymbol{\varepsilon}}^e + \dot{\boldsymbol{\varepsilon}}^p \tag{42}$$

4) Elastic constitutive equation (see Eq. (39)).

5) Consistency condition: As a stress point constantly exists on the yield surface in the elastoplastic state, all variables in the yield function must satisfy the following equation:

$$\dot{f} = \frac{\partial f}{\partial\boldsymbol{\sigma}'} : \dot{\boldsymbol{\sigma}}' + \frac{\partial f}{\partial p'_c}\dot{p}'_c + \frac{\partial f}{\partial p'_s}\dot{p}'_s = 0 \tag{43}$$

6) Hardening rule: Eqs. (12) and (13) provide the following equations:

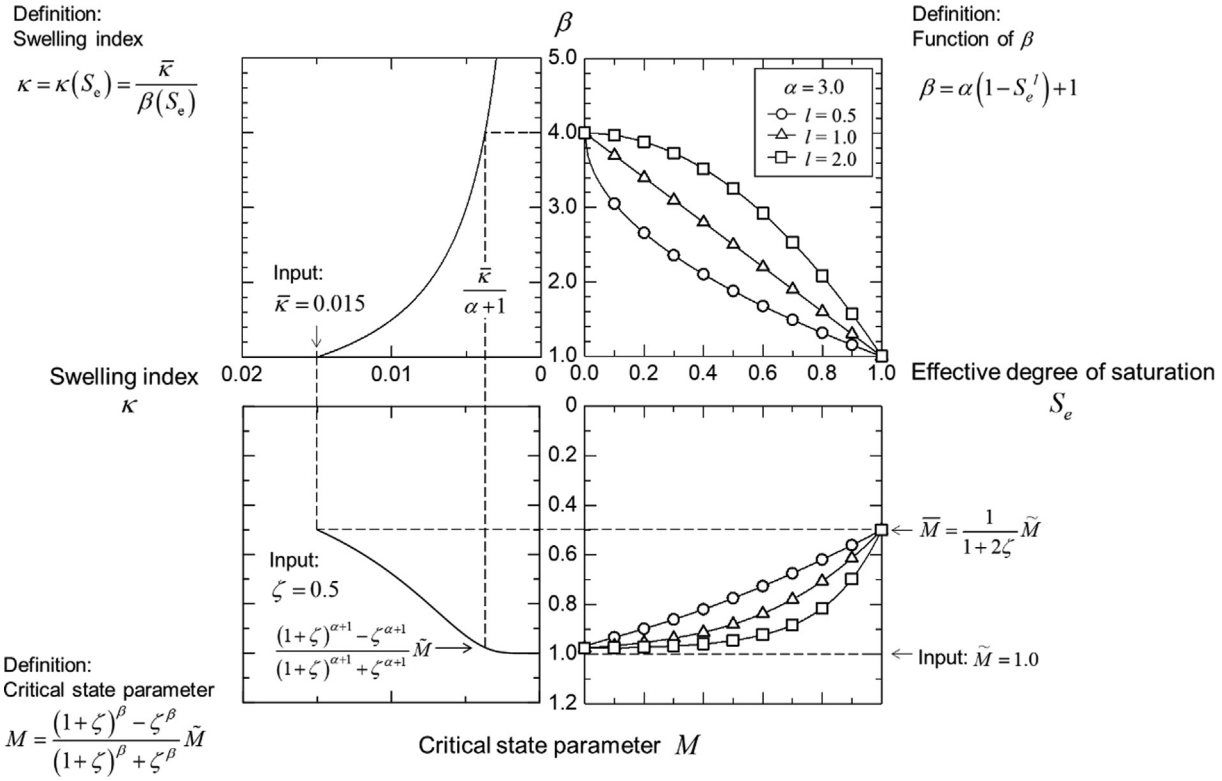

Fig. 7. Dependency of effective degree of saturation S_e on variable β, swelling index κ, and critical state parameter M.

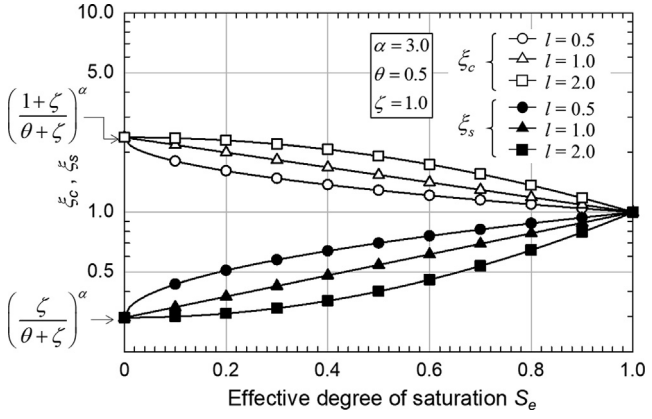

Fig. 8. Variations in ξ_c and ξ_s with effective degree of saturation.

$$\dot{p}'_c = \frac{\partial p'_c}{\partial \beta}\frac{\partial \beta}{\partial S_e}\dot{S}_e + \frac{\partial p'_c}{\partial \bar{p}'_c}\dot{\bar{p}}'_c \tag{44}$$

$$\dot{p}'_s = \frac{\partial p'_s}{\partial \beta}\frac{\partial \beta}{\partial S_e}\dot{S}_e + \frac{\partial p'_s}{\partial \bar{p}'_s}\dot{\bar{p}}'_s \tag{45}$$

By describing $\dot{\bar{p}}'_c$ and $\dot{\bar{p}}'_s$ in the same manner as Eq. (6), Eqs. (44) and (45) are, respectively, expressed as

$$\dot{p}'_c = H_{cs}\dot{S}_e + H_{ce}\dot{\varepsilon}^p_v \tag{46}$$

and

$$\dot{p}'_s = H_{ss}\dot{S}_e + H_{se}\dot{\varepsilon}^p_v \tag{47}$$

Individually,

$$H_{cs} = \frac{\partial p'_c}{\partial \beta}\frac{\partial \beta}{\partial S_e} = p'_c \ln\left(\frac{1+\zeta}{\theta+\zeta}\right)\frac{\partial \beta}{\partial S_e} \tag{48}$$

$$H_{ce} = \frac{\partial p'_c}{\partial \bar{p}'_c}\frac{1+e_{c0}}{\lambda-\kappa}\bar{p}'_c = \frac{1+e_{c0}}{\lambda-\kappa}p'_c \tag{49}$$

$$H_{ss} = \frac{\partial p'_s}{\partial \beta}\frac{\partial \beta}{\partial S_e} = p'_s \ln\left(\frac{\zeta}{\theta+\zeta}\right)\frac{\partial \beta}{\partial S_e} \tag{50}$$

$$H_{se} = \frac{\partial p'_s}{\partial \bar{p}'_s}\frac{1+e_{c0}}{\lambda-\kappa}\bar{p}'_s = \frac{1+e_{c0}}{\lambda-\kappa}p'_s \tag{51}$$

Substituting Eqs. (41) and (42) into Eq. (39) yields the following equation:

$$\dot{\boldsymbol{\sigma}}' = \boldsymbol{D}^e : \left(\dot{\boldsymbol{\varepsilon}} - \gamma\frac{\partial f}{\partial \boldsymbol{\sigma}'}\right) - K_{S_e}\dot{S}_e\boldsymbol{I} \tag{52}$$

By substituting Eq. (52) into $\dot{\boldsymbol{\sigma}}'$ in Eq. (43), Eq. (46) into $\dot{p}'_c$, and Eq. (47) into $\dot{p}'_s$, plastic multiplier γ can be obtained as follows:

$$\gamma = \frac{1}{H}\left[\frac{\partial f}{\partial \boldsymbol{\sigma}'} : \boldsymbol{D}^e : \dot{\boldsymbol{\varepsilon}} - \left(\frac{\partial f}{\partial p'}K_{S_e} - \frac{\partial f}{\partial p'_c}H_{cs} - \frac{\partial f}{\partial p'_s}H_{ss}\right)\dot{S}_e\right]. \tag{53}$$

Consequently, by substituting Eq. (53) into Eq. (52), the stress–strain relation in the elastoplastic state is described as

$$\dot{\boldsymbol{\sigma}}' = \boldsymbol{D}^{ep} : \dot{\boldsymbol{\varepsilon}} - \boldsymbol{D}_{S_e}\dot{S}_e \tag{54}$$

$$\boldsymbol{D}^{ep} = \boldsymbol{D}^{e} - \frac{1}{H}\left(\boldsymbol{D}^{e} : \frac{\partial f}{\partial \boldsymbol{\sigma}'} \otimes \frac{\partial f}{\partial \boldsymbol{\sigma}'} : \boldsymbol{D}^{e}\right) \tag{55}$$

$$\boldsymbol{D}_{S_e} = K_{S_e}\mathbf{1} - \frac{1}{H}\left(\frac{\partial f}{\partial p'}K^{S_e} - \frac{\partial f}{\partial p'_c}H_{cs} - \frac{\partial f}{\partial p'_s}H_{ss}\right)\boldsymbol{D}^{e} : \frac{\partial f}{\partial \boldsymbol{\sigma}'} \tag{56}$$

$$H = \frac{\partial f}{\partial \boldsymbol{\sigma}'} : \boldsymbol{D}^{e} : \frac{\partial f}{\partial \boldsymbol{\sigma}'} - \frac{\partial f}{\partial p'_c}H_{ce}\frac{\partial f}{\partial p'} - \frac{\partial f}{\partial p'_s}H_{se}\frac{\partial f}{\partial p'} \tag{57}$$

where $\boldsymbol{D}^{ep}$ is the elastoplastic stiffness tensor. The respective derivatives of yield function f, with respect to σ',p',p'_c, and p'_s, are.

$$\frac{\partial f}{\partial \boldsymbol{\sigma}'} = \frac{2p' - \left(p'_c + p'_s\right)}{3}\boldsymbol{I} + \frac{3}{\bar{M}^2}\boldsymbol{s} \tag{58}$$

$$\frac{\partial f}{\partial p'} = 2p' - \left(p'_c + p'_s\right) \tag{59}$$

$$\frac{\partial f}{\partial p'_c} = -\left(p' - p'_s\right) \tag{60}$$

$$\frac{\partial f}{\partial p'_s} = -\left(p' - p'_c\right) \tag{61}$$

3. Parameter estimation method

The constitutive model proposed in this paper has 10 parameters: compression index λ, swelling index $\bar{\kappa}$, critical state parameter $\bar{M}$, effective Poisson's ratio ν', reference combination on the NCL $\left(e_{ref}, p'_{ref}\right)$, plastic rebound parameter ζ, and unsaturated material parameters α,θ, and l. All the parameters, except for α,θ, and l, can be identified by one-dimensional consolidation tests and triaxial shear tests (Tachibana et al., 2020). As unsaturated material parameters α,θ, and l can control the effects of saturation on the NCL and PRL, it is possible to determine the parameters from the results of isotropic loading and unloading tests under controlled suction conditions. However, the number of such tests is insufficient. In comparison, numerous swelling pressure tests have been conducted to confirm the swelling properties of bentonite (Komine and Ogata, 1994; Börgesson et al., 1995; Lloret and Villar, 2007; Schanz and Tripathy, 2009; Ye et al., 2010). Accordingly, Section 3 proposes a method to estimate the unsaturated material parameters, i.e.,α,θ, and l, from the results of swelling pressure tests.

Firstly, this section describes a conditional expression in which the unsaturated material parameters should satisfy the saturation process by employing two assumptions:

1) The confining pressure at the beginning of the test is isotropically zero.

It is assumed that the specimen is removed from the compaction mold after the compaction process and placed in the swelling pressure test apparatus. Therefore, the axial and radial total stresses are equal to zero at the beginning of the test.

2) The swelling pressure at saturation is isotropic.

Tanaka and Watanabe (2019) assumed that the swelling pressure at saturation was isotropic. Conversely, Saba et al. (2014) and Jia et al. (2019) reported that the swelling pressure showed anisotropy. The ratios of axial pressure to radial pressure were obtained for different dry densities in these studies; they mainly exist within the range of 0.8–1.0. In this study, the swelling pressure at saturation,P_{swel}, is assumed to be isotropic to facilitate the formulation of a conditional expression.

To describe the change in effective stress from the initial (unsaturated) state to the saturated state, Eq. (7) is employed under the isotropic stress state and with pore air pressure p_a of zero, as follows:

$$p' = p + p_{suc};\ p = \mathrm{tr}\boldsymbol{\sigma}/3 \tag{62}$$

where p is the total mean stress and $\boldsymbol{\sigma}$ is the total stress tensor. From Assumption 1, the initial stress state can be given by $(p,p') = (0,p_{suc})$. Meanwhile, the stress state at saturation is $(p,p') = (P_{swel},P_{swel})$, based on Assumption 2), because suction stress p_{suc} is zero with the loss of suction. Figs. 9 and 10, respectively, present the two water retention curves (WRC) and the responses of the constitutive model in the $e - \ln p'$ space from the unsaturated state to the saturated state. The constant-volume condition provides the changes in effective mean stress with a constant void ratio in Cases A and B. The initial states of Cases A and B are located in between the NCL and PRL, corresponding to the initial value of the effective degree of saturation. As Case A has high water retention and high initial effective mean stress, the effective mean stress decreases with the contraction of the elastic domain due to saturation. In contrast, it increases upon saturation in Case B. The following equations indicate the relations for Lines (1)–(3) in Fig. 10 and other relations for dividing the conditional expression:

$$(1) : e_{c0} = e^{ini} - \kappa_{ini}\ln\frac{p'_{c0}}{p'^{ini}} \tag{63}$$

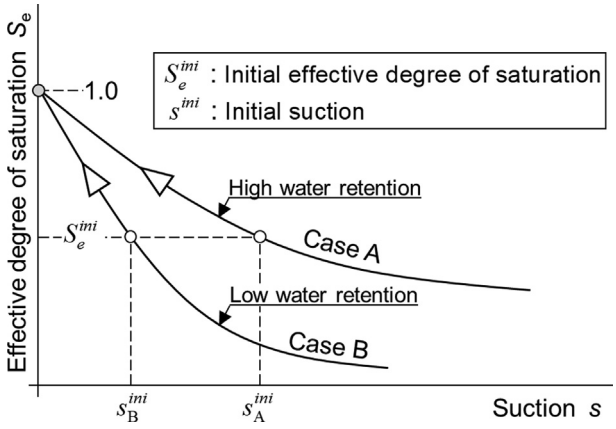

Fig. 9. Relationships between suction and effective degree of saturation during saturation.

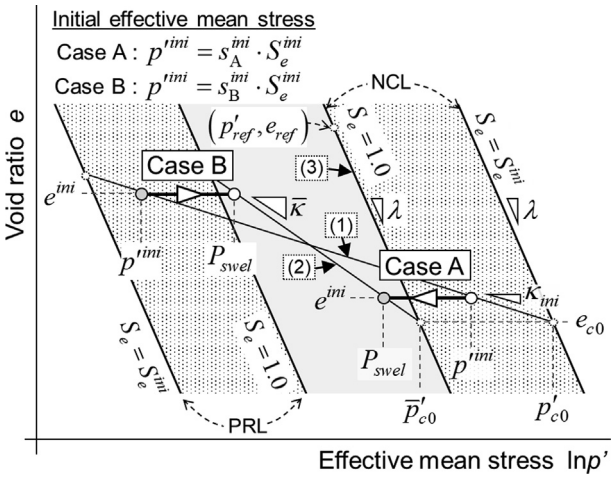

Fig. 10. Conceptual schematic of responses under constant volume condition during saturation.

$$(2): e_{c0} = e^{ini} - \bar{\kappa} \ln \frac{\bar{p}'_{c0}}{P_{swel}} \tag{64}$$

$$(3): e_{c0} = e_{ref} - \lambda \ln \frac{\bar{p}'_{c0}}{p'_{ref}} \tag{65}$$

$$\frac{p'_{c0}}{\bar{p}'_{c0}} = \exp[(\beta_{ini} - 1) \ln \frac{1+\zeta}{\theta+\zeta}] \tag{66}$$

$$\frac{\bar{\kappa}}{\kappa_{ini}} = \beta_{ini} \tag{67}$$

$$\beta_{ini} = \alpha \left\{ 1 - \left(S_e^{ini}\right)^l \right\} + 1 \tag{68}$$

By eliminating e_{c0} from Eqs. (63) and (64), the following relation is obtained:

$$\frac{e_{c0} - e^{ini}}{\bar{\kappa}} \left(\frac{\bar{\kappa}}{\kappa_{ini}} - 1 \right) + \ln \frac{p'_{c0}}{\bar{p}'_{c0}} - \ln \frac{p'^{ini}}{P_{swel}} = 0 \tag{69}$$

The elimination of $\bar{p}'_{c0}$ between Eqs. (64) and (65) results in the following equation:

$$e_{c0} = \frac{\lambda \bar{\kappa}}{\lambda - \bar{\kappa}} \ln \frac{P_{swel}}{p'_{ref}} + \frac{\lambda e^{ini} - \bar{\kappa} e_{ref}}{\lambda - \bar{\kappa}} \tag{70}$$

By substituting Eqs. (66) and (67) into Eq. (69), we have.

$$\beta_{ini} - 1 = \left(\ln \frac{p'^{ini}}{P_{swel}} \right) \Big/ \left(\ln \frac{1+\zeta}{\theta+\zeta} + \frac{e_{c0} - e^{ini}}{\bar{\kappa}} \right). \tag{71}$$

Finally, by substituting Eqs. (68) and (70) into Eq. (71), the conditional expression $g(\alpha, \theta, l) = 0$ is obtained as

$$g(\alpha, \theta, l) = \alpha \{ 1 - (S_e^{ini})^l \} - (\ln \tfrac{p'^{ini}}{P_{swel}}) / (h - \ln(\theta + \zeta)) = 0;$$

$$h = \ln(1+\zeta) + \frac{\lambda}{\lambda - \bar{\kappa}} \left(\ln \frac{P_{swel}}{p'_{ref}} - \frac{e_{ref} - e^{ini}}{\lambda} \right) \tag{72}$$

Fig. 11 shows the flow chart for the model parameters and the physical quantities at the initial state necessary for formulizing $g(\alpha, \theta, l) = 0$. As mentioned previously, the constitutive model parameters, $\lambda, \bar{\kappa}, e_{ref}, p'_{ref}$, and ζ, are determined by a consolidation test and a triaxial shear test. Furthermore, dry density ρ_d, initial water content w^{ini}, and equilibrium swelling pressure P_{swel} are clarified in swelling pressure tests. Therefore, initial void ratio e^{ini} and effective degree of saturation S_e^{ini} can be calculated from dry density ρ_d and initial water content ratio w^{ini} with soil particle density G_s. This study applies the logistic curve model proposed by Sugii and Uno (1996) to the WRC, as follows:

$$S_e = \frac{1}{1 + s^B \exp A} \tag{73}$$

where A and B are fitting parameters.

As $g(\alpha, \theta, l) = 0$ involves three unknown quantities, α, θ, and l, they must be determined by solving the conditional expressions with the swelling pressure test results for three different initial states. Swelling pressure tests are commonly performed on specimens with different dry densities and initial water content ratios, but made of the same material. Thus, the conditional expression for the three conditions can be easily formulated. The conditional expressions for the three test cases are given by.

$$g_1 = \alpha \{ 1 - (S_{e.1}^{ini})^l \} - (\ln \frac{p'^{ini}_1}{P_{swel.1}}) / (h_1 - \ln(\theta + \zeta)) = 0 \tag{74}$$

$$g_2 = \alpha \{ 1 - (S_{e.2}^{ini})^l \} - (\ln \frac{p'^{ini}_2}{P_{swel.2}}) / (h_2 - \ln(\theta + \zeta)) = 0 \tag{75}$$

$$g_3 = \alpha \{ 1 - (S_{e.3}^{ini})^l \} - (\ln \frac{p'^{ini}_3}{P_{swel.3}}) / (h_3 - \ln(\theta + \zeta)) = 0 \tag{76}$$

As the physical quantities used in $g(\alpha, \theta, l) = 0$ are dependent on the dry density and initial void ratio, they are denoted by a numerical subscript for each case.

By eliminating α from Eqs. (74) and (75), we have.

$$\ln(\theta+\zeta) - \frac{h_1 \left\{ 1 - \left(S_{e.1}^{ini}\right)^l \right\} \ln \frac{p'^{ini}_2}{P_{swel.2}} - h_2 \left\{ 1 - \left(S_{e.2}^{ini}\right)^l \right\} \ln \frac{p'^{ini}_1}{P_{swel.1}}}{\left\{ 1 - \left(S_{e.1}^{ini}\right)^l \right\} \ln \frac{p'^{ini}_2}{P_{swel.2}} - \left\{ 1 - \left(S_{e.2}^{ini}\right)^l \right\} \ln \frac{p'^{ini}_1}{P_{swel.1}}} = 0. \tag{77}$$

Similarly, the elimination of α between Eqs. (75) and (76) results in the following relation:

$$\ln(\theta+\zeta) - \frac{h_2 \{ 1 - (S_{e.2}^{ini})^l \} \ln \frac{p'^{ini}_3}{P_{swel.3}} - h_3 \{ 1 - (S_{e.3}^{ini})^l \} \ln \frac{p'^{ini}_2}{P_{swel.2}}}{\{ 1 - (S_{e.2}^{ini})^l \} \ln \frac{p'^{ini}_3}{P_{swel.3}} - \{ 1 - (S_{e.3}^{ini})^l \} \ln \frac{p'^{ini}_2}{P_{swel.2}}} = 0 \tag{78}$$

Finally, by eliminating $\ln(\theta + \zeta)$ from Eqs. (77) and (78), the following relation is derived:

$$F(l) = \sum_{i=1}^{3} \sum_{j=1}^{3} \sum_{k=1}^{3} e_{ijk} \{ 1 - (S_{e.i}^{ini})^l \} \{ 1 - (S_{e.j}^{ini})^l \} \times (\ln \frac{P_{swel.i}}{P_{swel.j}} + \frac{e_i^{ini} - e_j^{ini}}{\lambda}) \ln \frac{p'^{ini}_k}{P_{swel.k}} = 0 \tag{79}$$

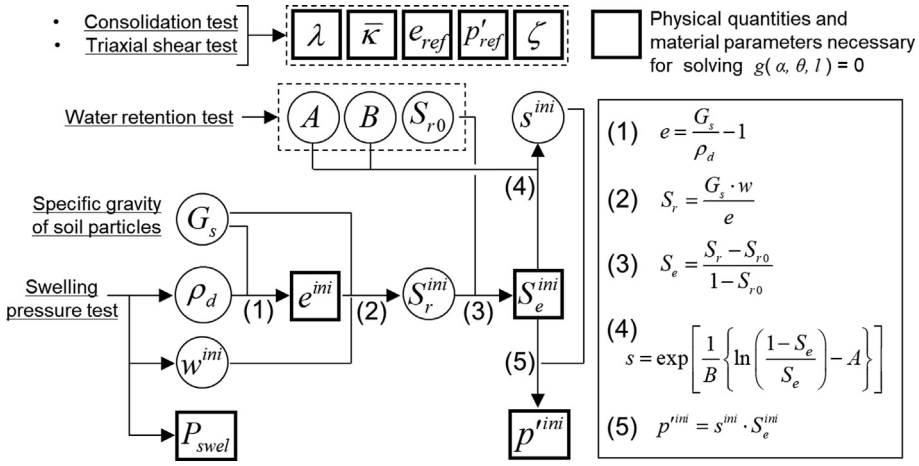

Fig. 11. Determination procedure for model parameters and physical quantities at initial state necessary for formulizing $g(\alpha,\theta,l)=0$.

After determining l from Eq. (79), the other parameters, α and θ, are determined by Eqs. (74) and (77), respectively.

Then, after determining the unsaturated material parameters, α,θ, and l, the parameter set must be confirmed to satisfy the following three conditions summarized in Fig. 12.

Condition (1): α,θ, and l should satisfy the range of each parameter.

Condition (2): The initial stress state should exist on or inside the yield surface. In each of the test cases, the initial value of the yield function f_{ini} calculated with the solutions for α,θ, and l should be negative or zero.

Condition (3): Any given effective mean stress between $(p^{'},S_e)=(p'^{ini},S_e^{ini})$ and $(p',S_e)=(P_{swel},1)$ under a constant void ratio can be obtained as follows:

$$p'(S_e)=\exp\left[\frac{1-S_e^{\,l}}{1-(S_e^{ini})^l}\ln p'^{\ ini}+\left(1-\frac{1-S_e^{\,l}}{1-(S_e^{ini})^l}\right)\ln P_{swel}\right] \tag{80}$$

By employing the WRC of Eq. (73), suction stress p_{suc} can be described as.

$$p_{suc}(S_e)=s\cdot S_e=S_e\cdot\exp\left[\frac{1}{B}\left\{\ln\left(\frac{1-S_e}{S_e}\right)-A\right\}\right] \tag{81}$$

By substituting Eqs. (80) and (81) into Eq. (62), the total mean stress under a constant void ratio can be expressed as.

$$\begin{aligned}p(S_e)=&exp\left[\frac{1-S_e^{\,l}}{1-(S_e^{ini})^l}\ln p'^{\ ini}+(1-\frac{1-S_e^{\,l}}{1-(S_e^{ini})^l})\ln P_{swel}\right]\\&-S_e\cdot\exp\left[\frac{1}{B}\{\ln(\frac{1-S_e}{S_e})-A\}\right].\end{aligned} \tag{82}$$

It can be seen from Eq. (82) that only l among the unsaturated material parameters affects the changes in the total mean stress with the effective degree of saturation. Fig. 13 shows examples of the development of swelling pressure with the effective degree of saturation S_e expressed by Eq. (82). As a negative value for the swelling pressure is not observed in the swelling pressure tests, the initial gradient of the total stress to the effective degree of saturation, $dpdS_e|_{S_e=S_e^{ini}}$, should be positive.

Ideally, the swelling pressure tests, whose results are used to estimate the three parameters,α,θ, and l, should have been carried out using a test apparatus designed to satisfy the condition that permits as little volume change of the specimen as possible, and the effect of the system compliance of the apparatus on the volume change should have been assessed.

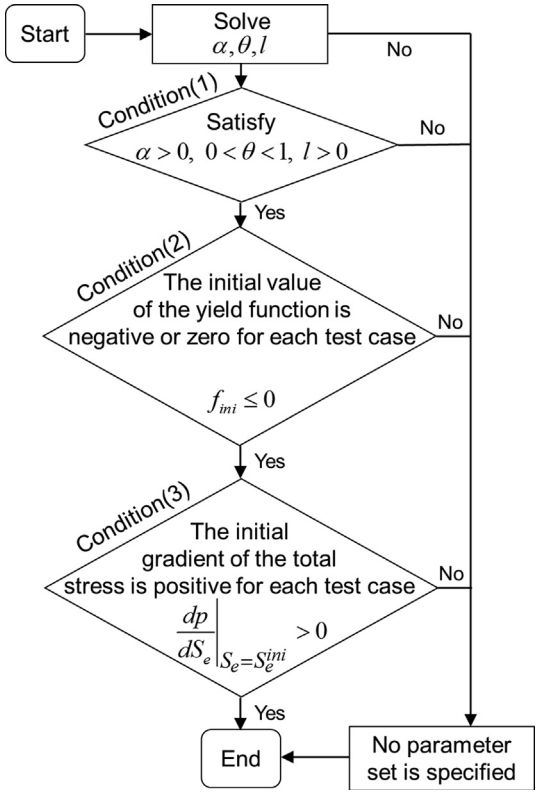

Fig. 12. Conditions that should be satisfied for unsaturated material parameters α,θ, and l.

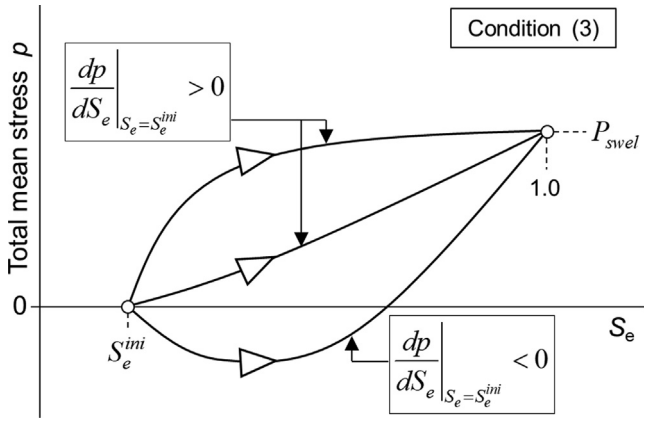

Fig. 13. Relationships between total mean stress and effective degree of saturation during saturation.

4. Parameter estimation for Kunigel V1

This section explains how the model parameters of Kunigel V1 (sodium-type bentonite) have been determined. Before the estimation of unsaturated material parameters α,θ, and l, by the method proposed in this study, the parameters for the constitutive model other than the unsaturated material parameters and the WRC are determined. Fig. 14 shows the results of the isotropic consolidation test on saturated Kunigel V1 conducted by Sasakura et al. (2003) and the calculated results. Compression index λ is determined by the gradient of the path from point 3 to point 4, which is regarded as the normally consolidated state in the compression path, and swelling index κ is determined by the gradient of the path from point 4 to point 5 in the initial unloading. The reference point on the NCL (e_{ref}, p'_{ref}) refers to point 4, while the location of the PRL is determined by setting the PRL to pass through point 1. The value of plastic rebound parameter ζ is calculated as the distance between the NCL and the PRL. The value of critical state parameter M is determined from the results of the triaxial undrained test conducted by Sasakura et al. (2003), and the value of effective Poisson's ratio ν is assumed to be 0.40.The water retention curves, with dry densities of 1.6 Mg/m^3 and 1.8 Mg/m^3, are determined from the results of the water retention test performed by Suzuki and Fujita (1999). Table 1 shows the parameters for the constitutive model and WRC model, as determined above.

Based on the methodology presented in the previous section, the remaining three parameters,α,θ, and l, are evaluated using the results of the swelling pressure tests conducted by Tanaka and Watanabe (2019). While they carried out swelling pressure tests using three test apparatuses with different stiffness levels, the test results used here were obtained using just one of them, i.e., a test apparatus that was carefully and meticulously designed to constrain the volume change of the specimen during the test as much as possible. Table 2 shows the experimental results for each case. The specimens had a height of 20 mm and a diameter of 60 mm; distilled water was supplied from the bottom under constant-volume conditions. Figs. 15 and 16 show the development of swelling pressure over time for each test case. Table 3 shows the initial values of the physical quantities necessary to achieve $g(\alpha, \theta, l) = 0$ for each test case. These physical quantities are calculated using the flow chart shown in Fig. 11. Fig. 17 shows the variation in the $F(l)$ value determined from Eq. (79) against l. As indicated in this figure, the unsaturated material parameter l that satisfies $F(l) = 0$ does not exist within the range of $l > 0$. As the calculation of other unsaturated material parameters, α and θ, requires the value of l, it is not possible to determine these parameters. Therefore, the conditions for the existence of a solution to $F(l) = 0$ are investigated by changing one of the three values for the equilibrium swelling pressure to be input, while allowing for its deviation from the actual measured value within the range shown in Table 4.

In Case 1, the values for the equilibrium swelling pressure in Test 1 are divided into 0.1% intervals in the range of −10% (1.73 MPa) to + 10% (2.11 MPa), whereas those for Tests 2 and 3 use the values given in Table 2. As with

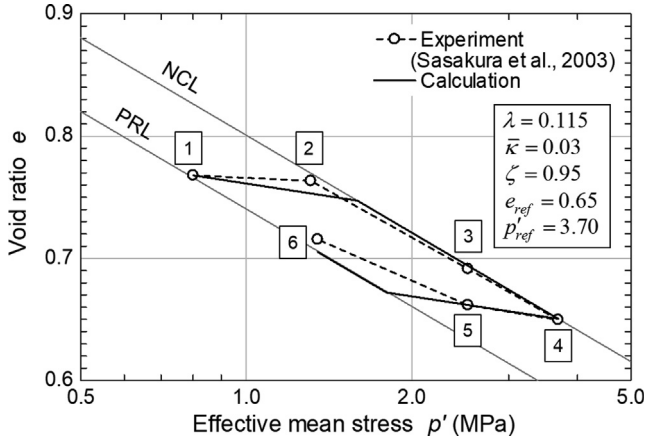

Fig. 14. Comparison of calculated and experimental results of isotropic consolidation test on Kunigel V1 (Sasakura et al., 2003).

Table 1
Model parameters for Kunigel V1.

Parameters for constitutive model			
λ	Compression index	-	0.115
$\bar{\kappa}$	Swelling index at saturated state	–	0.03
M	Critical state parameter	–	0.491
ζ	Plastic rebound parameter	–	0.95
ν'	Effective Poisson's ratio	–	0.40
e_{ref}	Reference combination on NCL	–	0.65
p'_{ref}		MPa	3.70

Parameters for WRC				
			Dry density (Mg/m^3)	
			1.6	1.8
A	Fitting parameters	–	−3.10	−3.95
B		–	1.0	1.0
S_{r0}	Residual degree of saturation	–	0.1	0.1

Table 2
Experimental data of swelling pressure tests on Kunigel V1 reported by Tanaka and Watanabe (2019).

No.	Dry density ρ_d (Mg/m^3)	Initial water content w^{ini}(%)	Equilibrium swelling pressure P_{swel} (MPa)
1	1.599	9.53	1.92
2	1,582	19.81	1.73
3	1.805	9.98	10.64

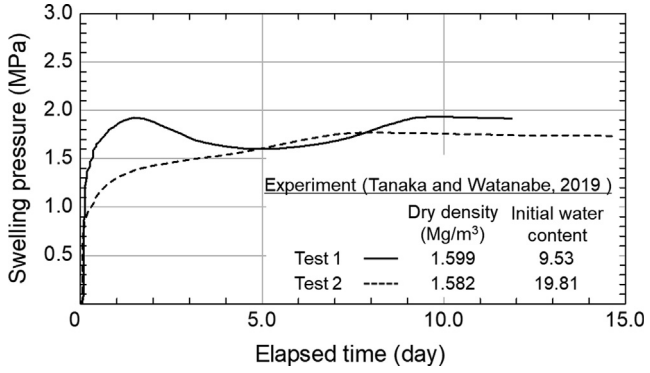

Fig. 15. Development of swelling pressure with elapsed time in Tests 1 (solid line) and 2 (broken line) reported by Tanaka and Watanabe (2019).

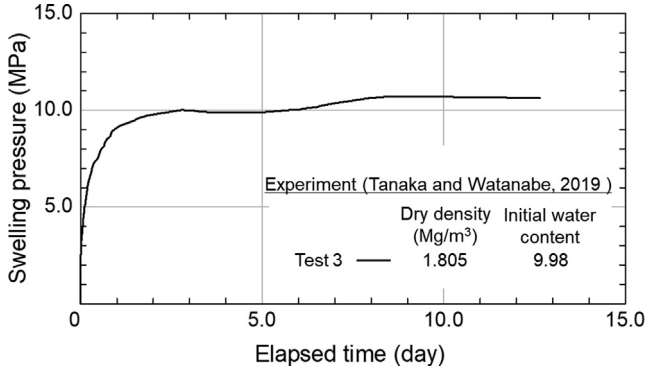

Fig. 16. Development of swelling pressure with elapsed time in Test 3 reported by Tanaka and Watanabe (2019).

Case 1, Case 2 and Case 3 are allowed to have certain ranges of equilibrium swelling pressure values, respectively, in Tests 2 and 3, while the other tests have fixed equilibrium swelling pressure values. The results of the parameter searching in Cases 1, 2, and 3 are shown in Figs. 18, 19, and 20, respectively. In Case 1, as $F(l)=0$ cannot be solved between -10.0% and $+1.5\%$,α,θ, and l cannot be determined. $F(l)=0$ can be solved between $+1.5\%$ and

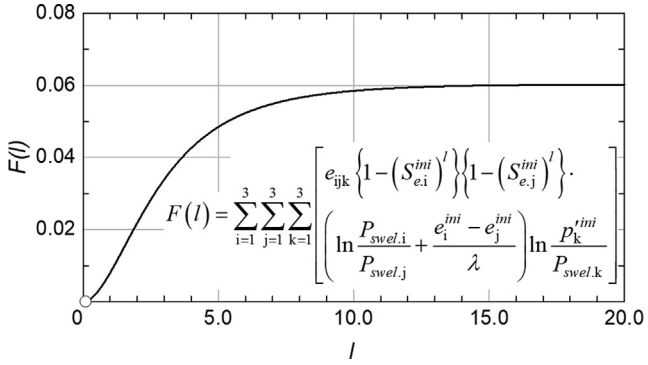

Fig. 17. Relationship between $F(l)$ and l.

$+5.0\%$, and between $+8.6\%$ and $+10.0$; however, Conditions (3) and (2) are violated, respectively. In Case 2, $F(l)=0$ cannot be solved between -10.0% and -8.1% or between -5.2% and $+10.0\%$. Although α,θ, and l can be determined between -8.1% and -5.2%, Condition (1) is violated. In Case 3, $F(l)=0$ cannot be solved between -1.6% and $+8.6\%$, and the determined α,θ, and l violate Conditions (3) and (1), respectively, between -10.0% and -1.6%, and between -8.6% and $+10.0\%$. After all, the range for which $F(l)=0$ can be solved and the solution which satisfies the three conditions explained in Fig. 12 are found within an error range of $+5.0\%$ and $+8.6\%$ for only Case 1. The unsaturated material parameters that can be obtained in this range are distributed as shown in Fig. 18. The equilibrium swelling pressures calculated with these parameter sets agree with the swelling pressures measured in Tests 2 and 3, but are slightly larger than the measured value in Test 1. Although there are slight differences between the calculated pressure and the measured pressure in Test 1, these parameter sets generally succeed in reproducing the equilibrium swelling pressure dependent on the dry density and the water content of each test. In order to determine which of the distributed parameter sets is the optimum, it is necessary to pay attention not only to the

Table 3
Initial value of physical quantities for each test case.

No.	Void ratio e^{ini}	Effective degree of saturation S_e^{ini}	Effective mean stress p'^{ini} (MPa)
1	0.716	0.295	15.66
2	0.735	0.711	6.41
3	0.520	0.474	27.33

Table 4
Modified values of equilibrium swelling pressure for estimating parameters.

Case	Equilibrium swelling pressure in Test 1 $P_{swel.1}$ (MPa)	Equilibrium swelling pressure in Test 2 $P_{swel.2}$ (MPa)	Equilibrium swelling pressure in Test 3 $P_{swel.3}$ (MPa)
1	[1.73, 2.11]	1.73	10.64
2	1.92	[1.56, 1.90]	10.64
3	1.92	1.73	[9.58, 11.70]

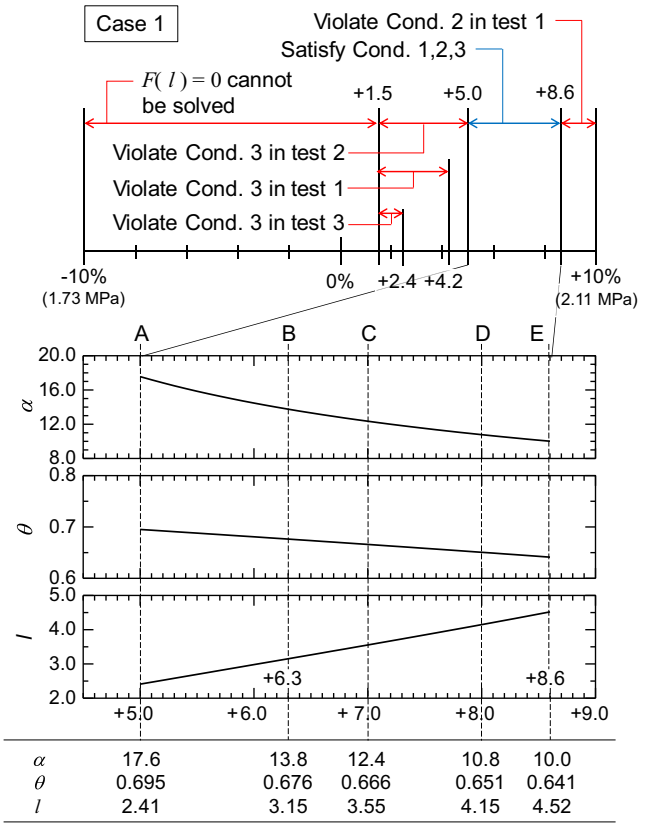

Fig. 18. Results of parameter searching in Case 1.

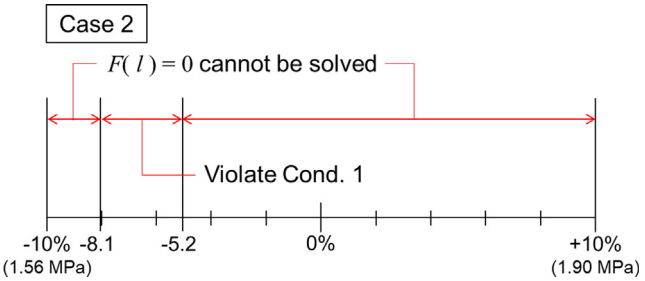

Fig. 19. Results of parameter searching in Case 2.

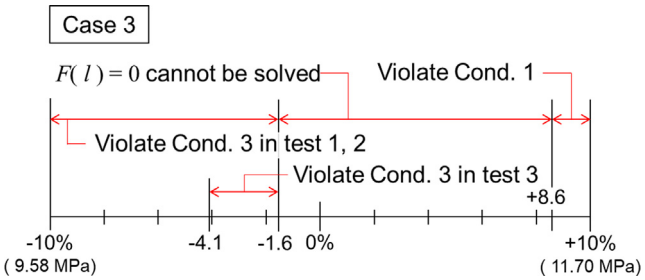

Fig. 20. Results of parameter searching in Case 3.

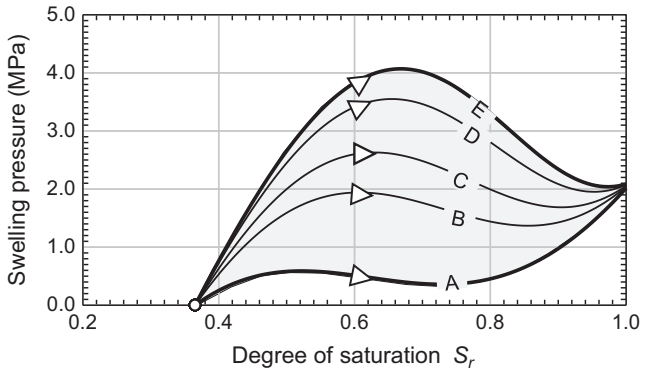

Fig. 21. Calculated results of changes in swelling pressure for Test 1 with five sets of parameters.

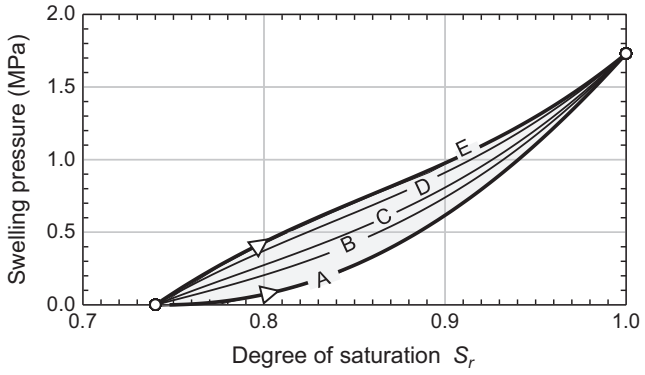

Fig. 22. Calculated results of changes in swelling pressure for Test 2 with five sets of parameters.

equilibrium swelling pressure, but also to the change in swelling pressure in the process of saturation.

Figs. 21, 22, and 23 show the changes in swelling pressure for Tests 1, 2, and 3, respectively, calculated from Eq. (82) using five sets of parameters (A to E) selected from the myriad of parameter sets shown in Fig. 18. In Test 1, as the value of l is increased, the swelling pressure increases more rapidly from the initial state. The swelling pressure decreases after it increases, and its value at this point varies depending on the value of l. After the degree of saturation increases further, the swelling pressure increases again. As shown in Eq. (62), the total stress (swelling pressure) is

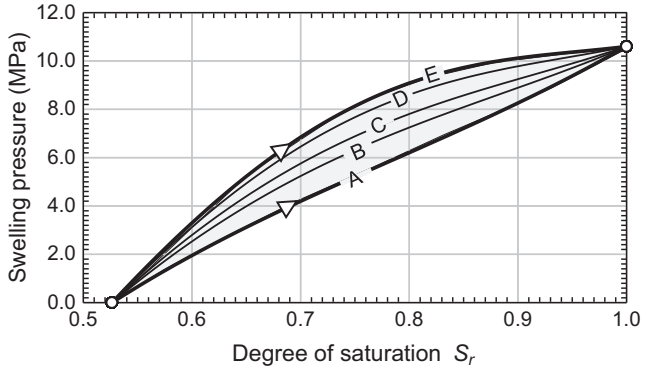

Fig. 23. Calculated results of changes in swelling pressure for Test 3 with five sets of parameters.

defined as the difference between the effective mean stress and the suction stress, so the increment in swelling pressure is calculated by the increment in effective mean stress,$\Delta p'$, and the increment in suction stress,Δp_{suc}. As the swelling pressure increases, $\Delta p'$ and Δp_{suc} satisfy the relation $\Delta p' > \Delta p_{suc}$, while they satisfy the relation $\Delta p' < \Delta p_{suc}$ as the swelling pressure decreases. As the change in effective mean stress increment $\Delta p'$ depends on parameter l, the increase and decrease in swelling pressure and the degree of saturation when the relationship between $\Delta p'$ and Δp_{suc} is switched also depends on parameter l. In Tests 2 and 3, the swelling pressure monotonically increases with an increase in the degree of saturation. The greater the value of l, the more rapidly the swelling pressure increases. The changes in variables β,ξ_c, and ξ_s with increasing saturation are shown in Fig. 24 when parameter sets A and E, which give the upper and lower limits of each parameter, are used within the parameter sets shown in Fig. 18. A and E are parameter sets which calculate approximately the same equilibrium swelling pressure if the initial conditions are the same. Among such parameter sets, the smaller parameter l is, such as A, the larger the value of variable β will be for the same degree of saturation compared with the other parameter sets, and hence, the smaller the occurrence of swelling pressure during saturation tends to be, as shown in Figs. 21 to 23. For reference, the relationship between the degree of saturation and suction, assumed when calculating the swelling pressure, is shown in Fig. 25. Although the assumed soil–water retention characteristics result in slightly larger suction, when compared to the plots obtained from the water retention tests by Suzuki and Fujita (1999), it is generally possible to reproduce the decrease in suction with increasing saturation, depending on the dry density of each test.

Only one parameter set (α, θ, l) for the validation of the proposed constitutive model is selected by comparing the experimental and calculated peak values of the swelling pressure in Test 1. As the specimen becomes saturated from the bottom up in this test, the swelling pressure in the test must be compared with the calculated pressure as a solution to the boundary value problem by using a numerical analysis method, such as the finite element method. However, the degree of saturation in the specimen in this study is assumed to increase uniformly, and the simulation for the validation employs a parameter set (α, θ, l) that enables the model to express the peak value measured in the laboratory test. Therefore, it is determined as $(\alpha, \theta, l) = (13.8, 0.676, 3.15)$, as shown in Fig. 18. Furthermore, the relation between the degree of saturation and the swelling pressure with this parameter set is described by the red lines in Figs. 21, 22, and 23.

The proposed parameter estimation method is sometimes unable to determine a parameter set (α, θ, l) which can exactly represent the three different measured values

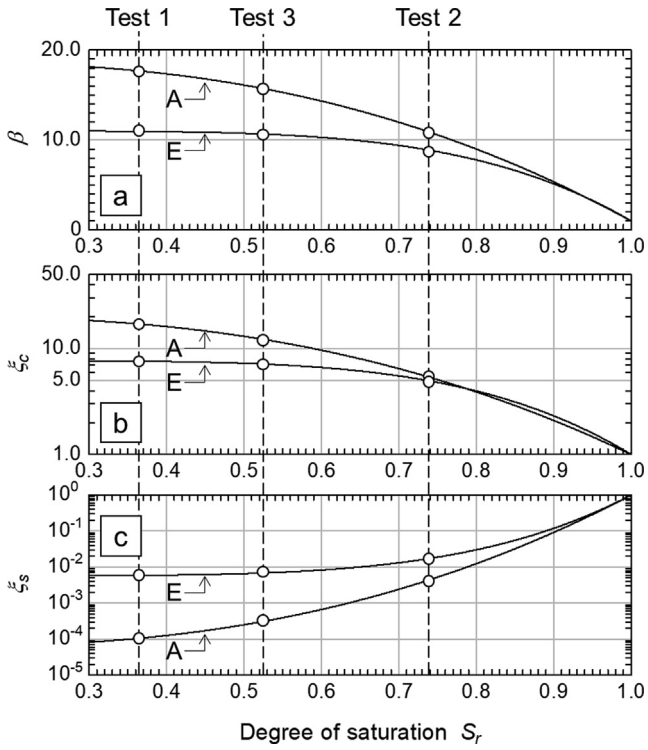

Fig. 24. Variations in variables: (a)β, (b)ξ_c, and (c) ξ_s with degree of saturation S_r.

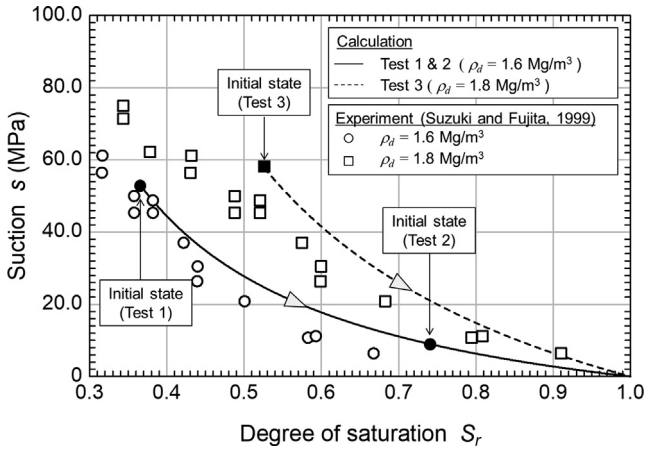

Fig. 25. Variations in suction s with degree of saturation S_r in computed and experimental results.

of the equilibrium swelling pressure. In such cases, it is necessary to search the parameters until a solution is found, while allowing for deviation from the actual measured value of at least one of the three measured values. If more than one set of parameters can be found, it is necessary to select one of them by comparing their peak values, as in this paper, or by validating its reproducibility against swelling deformation tests.

5. One-dimensional swelling deformation simulation

Oguri et al. (2012) investigated the effects of the initial dry density and vertical load on the one-dimensional deformation characteristics of Kunigel V1 during the saturation process. The specimens were compacted at water contents of 7.65–9.28% to the prescribed dry densities of 1.6 and 1.8 Mg/m^3, and had a diameter of 60 mm and a height of 10 mm. Distilled water was supplied from the bottom of the specimens under a constant vertical stress between 1.0 and 10.0 MPa until reaching full saturation. Figs. 26 and 27 show the changes in dry densities for each vertical stress.

The one-dimensional swelling deformation simulation was conducted by the numerical scheme described in the Appendix. Table 1 lists the parameters for the constitutive model and the WRC model. Although it is desirable to apply the WRC model by considering its dependency on the dry density to predict the change in dry density of the specimen during saturation in the swelling deformation test, the WRCs corresponding to the initial dry densities are employed. The combination of the unsaturated material parameters $(\alpha, \theta, l) = (13.8, 0.676, 3.15)$, estimated in the previous chapter, is used. Tables 5 and 6 show the initial conditions in the simulation. It should be noted that, since the initial water content of each specimen was not specified in the referenced experiment, the average value (8.5%) of the range in water content in the experiment is used for the initial condition of the simulation. Furthermore, the initial radial total stress is assumed to be equal to the axial total stress.

Figs. 28 and 29 plot the simulated results for looser and denser samples, respectively, with exactly the same initial

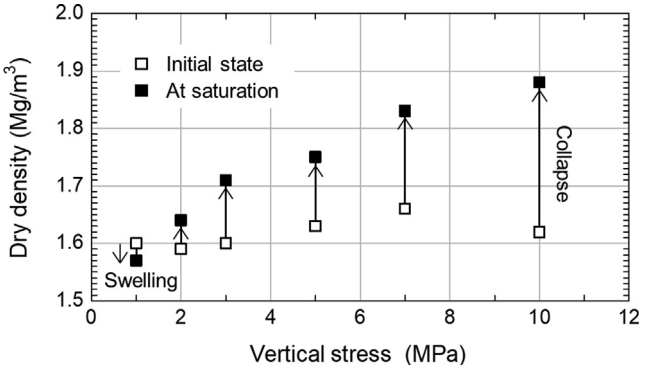

Fig. 26. Change in dry density for each vertical stress reported by Oguri et al. (2012) (Initial dry density: approximately 1.6 Mg/m^3).

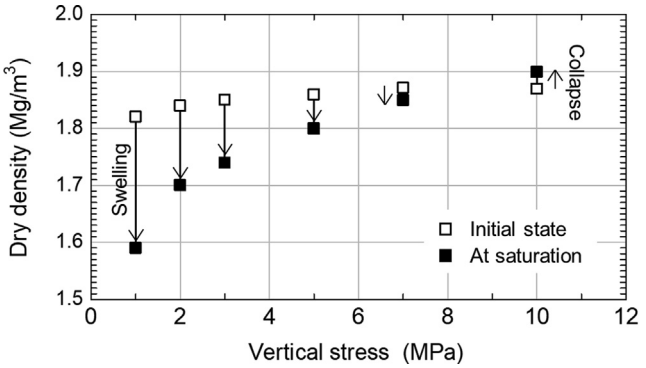

Fig. 27. Change in dry density for each vertical stress reported by Oguri et al. (2012) (Initial dry density: approximately 1.8 Mg/m^3).

Table 5
Initial conditions for one-dimensional swelling deformation simulation on Kunigel V1 (Initial dry density: approximately 1.6 Mg/m^3).

Vertical stress σ_v (MPa)	Initial dry density ρ_d^{ini} (Mg/m^3)	Initial degree of saturation S_r^{ini}
1	1.60	0.326
2	1.59	0.321
3	1.60	0.326
5	1.63	0.341
7	1.66	0.357
10	1.62	0.336

Table 6
Initial conditions for one-dimensional swelling deformation simulation on Kunigel V1 (Initial dry density: approximately 1.8 Mg/m^3).

Vertical stress σ_v (MPa)	Initial dry density ρ_d^{ini} (Mg/m^3)	Initial degree of saturation S_r^{ini}
1	1.82	0.459
2	1.84	0.475
3	1.85	0.483
5	1.86	0.490
7	1.87	0.499
10	1.87	0.499

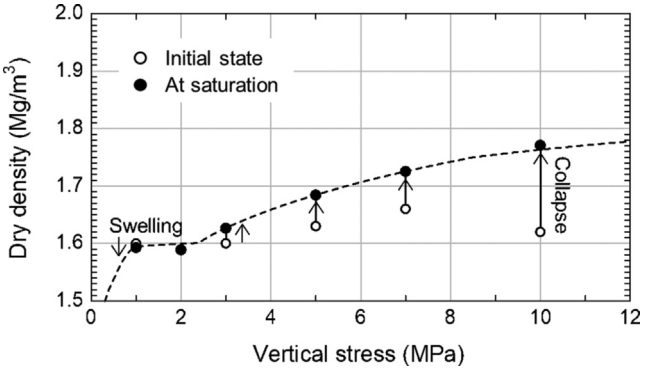

Fig. 28. Simulated results of one-dimensional swelling deformation tests. Plots show results with exactly the same initial dry densities as those in the experiment by Oguri et al. (2021). Broken line shows a series of results with the initial dry density of 1.6 Mg/m^3 and initial water content of 8.5%.

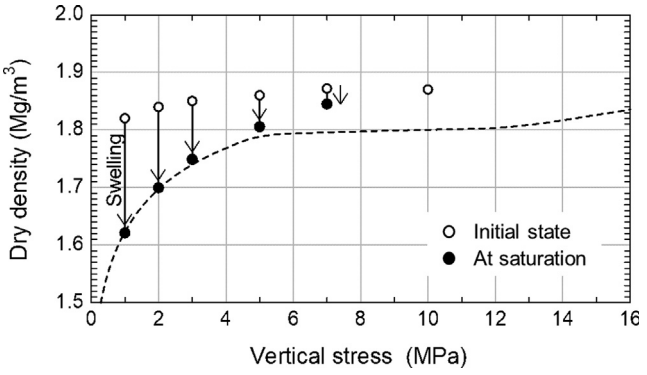

Fig. 29. Simulated results of one-dimensional swelling deformation tests. Plots show results with exactly the same initial dry densities as those in the experiment by Oguri et al. (2021). Broken line shows a series of results with the initial dry density of 1.8 Mg/m^3 and initial water content of 8.5%.

dry densities as those used in the experiment by Oguri et al. (2021). In the figures, the series of simulated results with given initial dry densities (1.6 Mg/m^3 in Fig. 28 and 1.8 Mg/m^3 in Fig. 29) are represented as dashed lines. As shown in Fig. 28, the broken line indicates that the transition stress between swelling and collapse (in other words, a stress where no volume change occurs even when water is absorbed) is about 1.0–2.0 MPa. Thus, at the relatively low dry density of about 1.6 Mg/m^3, the material swells at a lower vertical stress than 1.0 MPa, but contracts when the vertical stress exceeds 2.0 MPa. The calculation results show that the higher the vertical stress above this transition stress, the greater the collapse, which is consistent with the experimental results shown in Fig. 26. On the other hand, at the relatively high dry density of about 1.8 Mg/m^3, shown in Fig. 29, a large amount of swelling occurs at low vertical stress, but the amount of swelling tends to decrease as the stress increases. Since the transition stress at the initial dry density of 1.8 Mg/m^3 is about 8–12 MPa, the vertical stresses below 8 MPa shown here result in the swelling of the material, and there is almost no volume change at 10 MPa.

The influence of dry density and vertical stress on the swelling and collapse behavior of some bentonite materials was also investigated in other studies (e.g., Villar, 2005; Sun et al., 2014). The constitutive model proposed in this study can be applied to Kunigel V1 and other bentonite materials because the test results reported from those examinations present trends similar to those observed in the simulated results from this study.

6. Conclusion

To predict the mechanical behavior of expansive soils due to saturation, a constitutive model incorporating the concept of plastic rebound was investigated in this study by employing the existing framework of the constitutive model for unsaturated soil. Additionally, this study proposed a method to estimate the constitutive model parameters using material characteristics obtained by swelling pressure tests. As swelling pressure tests have been implemented for various expansive soils, the method proposed here can be applied by utilizing the existing test results. Although the unsaturated material parameters were estimated by a conditional expression under a constant volume, the simulated results confirmed that the constitutive model proposed in this study can express the development of swelling pressure due to saturation and reproduce the deformation characteristics with various vertical loads by utilizing the estimated parameters. The proposed model can contribute to the evaluation of the behavior of the bentonite buffer in repositories by providing predictions of the changes in dry densities and stress states under groundwater infiltration.

Acknowledgement

The authors wish to thank Professor Hideki Ohta for his helpful support and encouragement.

Appendix. The equations for the one-dimensional swelling deformation simulation are the constitutive equation, the WRC model, and the effective stress equation. The incremental forms of Eqs. (39) and (54) are employed under the axisymmetric condition, as follows:

$$\begin{Bmatrix} \Delta\sigma'_a \\ \Delta\sigma'_r \end{Bmatrix} = \begin{bmatrix} D_{aa} & D_{ar} \\ D_{ra} & D_{rr} \end{bmatrix} \begin{Bmatrix} \Delta\varepsilon_a \\ \Delta\varepsilon_r \end{Bmatrix} - \begin{Bmatrix} D_a^{S_e} \\ D_r^{S_e} \end{Bmatrix} \Delta S_e \tag{A1}$$

where D_{aa},D_{ar},D_{ra}, and D_{rr} are stiffness coefficients. Axial effective stress σ'_a and radial effective stress σ'_r correspond to the effective stress tensor components, as follows:

$$\sigma'_a = \sigma'_{22},\ \sigma'_r = \sigma'_{11} = \sigma'_{33} \tag{A2}$$

Similarly, axial strain ε_a and radial strain ε_r are expressed as.

$$\varepsilon_a = \varepsilon_{22},\ \varepsilon_r = \varepsilon_{11} = \varepsilon_{33} \tag{A3}$$

Therefore, the stiffness coefficients can be described as.

$$D_{aa} = D_{2222}, D_{ar} = D_{2211} + D_{2233} \tag{A4}$$

$$D_{ra} = D_{1122},\ D_{rr} = D_{1111} + D_{1133} \tag{A5}$$

Eq. (40) is applied to the components of stiffness tensor $\boldsymbol{D}$ in the elastic state, whereas Eq. (55) is employed in the elastoplastic state. $D_a^{S_e}$ and $D_r^{S_e}$ are described, respectively, as follows:

$$D_a^{S_e} = D_r^{S_e} = K_{S_e}\ (Elastic\ state) \tag{A6}$$

$$D_a^{S_e} = D_{22}^{S_e},\ D_r^{S_e} = D_{11}^{S_e}\ (Elastoplastic\ state) \tag{A7}$$

The WRC model of Eq. (73) is employed in the incremental form, as follows:

$$\Delta S_e = \frac{(Bs^{B-1})\exp A}{(1+s^B \exp A)^2}\Delta s \tag{A8}$$

The incremental form of the effective stress equation in Eq. (7) can be obtained with pore air pressure p_a of zero and under the axisymmetric condition, as follows:

$$\begin{Bmatrix} \Delta\sigma'_a \\ \Delta\sigma'_r \end{Bmatrix} = \begin{Bmatrix} \Delta\sigma_a \\ \Delta\sigma_r \end{Bmatrix} + \Delta s \begin{Bmatrix} S_e \\ S_e \end{Bmatrix} + \Delta S_e \begin{Bmatrix} s \\ s \end{Bmatrix} \tag{A9}$$

where σ_a is the axial total stress and σ_r is the total radial stress. Increments in the unknown physical quantities are calculated by solving Eqs. (A1), (A8), and (A9) simultaneously with a given value for the suction increment, a radial strain increment of zero, and a axial total stress increment of zero. Then, the values for each physical quantity are updated. The computation steps are iterated until the value for suction reaches zero.

References

Alonso, E.E., Vaunat, J., Gens, A., 1999. Modelling the mechanical behaviour of expansive clays. Eng. Geol. 54 (1-2), 173–183.

Alonso, E.E., Gens, A., Josa, A., 1990. A constitutive model for partially saturated soils. Géotechnique 40 (3), 405–430.

Amerasinghe, S.F., Kraft, L.M., 1983. Application of a Cam-clay model to overconsolidated clay. Int. J. Numer. Anal. Meth. Geomech. 7 (2), 173–186.

Bishop, A.W., 1959. The principle of effective stress. Teknisk Ukeblad 106 (39), 859–863.

Börgesson, L., Johannesson, L.-E., Sanden, T., Hernelind, J., 1995. Modelling of the physical behaviour of water saturated clay barriers. Svensk Kärnbränslehantering AB.

Dupray, F., François, B., Laloui, L., 2013. Analysis of the FEBEX multi-barrier system including thermoplasticity of unsaturated bentonite. Int. J. Numer. Anal. Meth. Geomech. 37 (4), 399–422.

Guimarães, N., Gens, A., Sánchez, M., Olivella, S., 2013. A chemo-mechanical constitutive model accounting for cation exchange in expansive clays. Géotechnique 63 (3), 221–234.

Jia, L.-Y., Chen, Y.-G., Ye, W.-M., Cui, Y.-J., 2019. Effects of a simulated gap on anisotropic swelling pressure of compacted GMZ bentonite. Eng. Geol. 248, 155–163.

Karube, D., Kawai, K., 2001. The role of pore water in the mechanical behavior of unsaturated soils. Geotech. Geol. Eng. 19, 211–241.

Kobayashi, I., Toida, M., Sasakura, T., Ohta, H., 2007. Interpretation of compression/swelling behavior of compacted bentonite using constant water-content line and constant degree of saturation line. J. Geotech. Eng. 63 (4), 1065–1078, in Japanese.

Kohgo, Y., Nakano, M., Miyazaki, T., 1993. Theoretical aspects of constitutive modelling for unsaturated soils. Soils Found. 33 (4), 49–63.

Komine, H., Ogata, N., 1994. Experimental Study on Swelling Characteristics of Compacted Bentonite. Can. Geotech. J. 31 (4), 478–490.

Komine, H., Ogata, N., 1996. Prediction for swelling characteristics of compacted bentonite. Can. Geotech. J. 33 (1), 11–22.

Komine, H., Watanabe, Y., 2010. The past, present and future of the geoenvironment in Japan. Soils Found. 50 (6), 977–982.

Kyokawa, H., Ohno, S., Kobayashi, I., 2020. A method for extending a general constitutive model to consider the electro-chemo-mechanical phenomena of mineral crystals in expansive soils. Int. J. Numer. Anal. Met. 44 (6), 749–771.

Li, W., Yang, Q., 2017. A macro-structural constitutive model for partially saturated expansive soils. B. Eng. Geol. Environ. 76 (3), 1075–1084.

Lloret, A., Villar, M.V., 2007. Advances on the knowledge of the thermo-hydro-mechanical behaviour of heavily compacted "FEBEX" bentonite. Phys. Chem. Earth Parts A/B/C 32 (8-14), 701–715.

Mašín, D., 2013. Double structure hydromechanical coupling formalism and a model for unsaturated expansive clays. Eng. Geol. 165, 73–88.

Oguri, H., Komine, H., Murakami, S., 2012. Effect of initial dry density on the one-dimensional deformation characteristics of unsaturated bentonite during the saturation process. Proceedings of 67th Annual Meeting of Japanese Society of Civil Engineers, CS13-005, pp. 9-10 (in Japanese).

Ohno, S., Kawai, K., Tachibana, S., 2007. Elasto-plastic constitutive model for unsaturated soil applied effective degree of saturation as a parameter expressing stiffness. J. JSCE 63 (4), 1132–1141, in Japanese.

Pusch, R., 1979. Highly compacted sodium bentonite for isolating rockdeposited radioactive waste products. Nucl. Technol. 45 (2), 153–157.

Romero, E., Simms, P.H., 2008. Microstructure investigation in unsaturated soils: a review with special attention to contribution of mercury intrusion porosimetry and environmental scanning electron microscopy. Geotech. Geol. 26 (6), 705–727.

Roscoe, K.H., Burland, J.H., 1968. On the generalized stress-strain behavior of 'wet' clay. In: Heyman, J., Leckie, F.A. (Eds.), Engineering Plasticity. Cambridge Univ, Press, pp. 535–609.

Saba, S., Barnichon, J.-D., Cui, Y.-J., Tang, A.M., Delage, P., 2014. Microstructure and anisotropic swelling behaviour of compacted bentonite/sand mixture. J. Rock Mech. Geotech. Eng. 6 (2), 126–132.

Sasakura, T., Kuroyanagi, M., Kobayashi, I., Okamoto, M., 2003. Studies on mechanical behaviour of bentonite for development of the constitutive model II. Report of Japan Nuclear Cycle Development Institute, JNC, TJ8400 2003–048 (in Japanese.

Schanz, T., Khan, M.I., Al-Badran, Y., 2013. An alternative approach for the use of DDL theory to estimate the swelling pressure of bentonites. Appl. Clay Sci. 83-84, 383–390.

Schanz, T., Tripathy, S., 2009. Swelling pressure of a divalent-rich bentonite: Diffuse double-layer theory revisited. Water Resour. Res. 45 (5). https://doi.org/10.1029/2007WR006495.

Seiphoori, A., Ferrari, A., Laloui, L., 2014. Water retention behaviour and microstructural evolution of MX-80 bentonite during wetting and drying cycles. Géotechnique 64 (9), 721–734.

Sheng, D., 2011. Review of fundamental principles in modelling unsaturated soil behaviour. Comput. Geotech. 38 (6), 757–776.

Sugii, T., Uno, T., 1996. Modeling of hydraulic properties for unsaturated soils. Proc. Symp. Permeability of Unsaturated Ground, Japan, 179–184, in Japanese.

Sun, D., Sun, W., Fang, L., 2014. Swelling characteristics of Gaomiaozi bentonite and its prediction. J. Rock Mech. Geotech. Eng. 6 (2), 113–118.

Sun, W., Sun, D., 2012. Coupled modelling of hydro-mechanical behaviour of unsaturated compacted expansive soils. Int. J. Numer. Anal. Meth. Geomech. 36 (8), 1002–1022.

Suzuki H., and Fujita T., 1999. Unsaturated hydraulic property of buffer material, Report of Japan Nuclear Cycle Development institute, JNC TN8430 99-010 (in Japanese)

Sánchez, M., Gens, A., do Nascimento Guimarães, L., Olivella, S., 2005. A double structure generalized plasticity model for expansive materials. Int. J. Numer. Anal. Meth. Geomech. 29 (8), 751–787.

Sánchez, M., Gens, A., Villar, M.V., Olivella, S., 2016. Fully coupled thermo-hydro-mechanical double-porosity formulation for unsaturated soils. Int. J. Geomech. 16 (6). https://doi.org/10.1061/(ASCE)GM.1943-5622.0000728.

Tachibana, S., Ito, S., Iizuka, A., 2020. Constitutive model with a concept of plastic rebound for expansive soils. Soils Found. Soils Found. 60 (1), 179–197.

Takayama, Y., Tachibana, S., Iizuka, A., Kawai, K., Kobayashi, I., 2017. Constitutive modeling for compacted bentonite buffer materials as unsaturated and saturated porous media. Soils Found. 57 (1), 80–91.

Tanaka, Y., Watanabe, Y., 2019. Modelling the effects of test conditions on the measured swelling pressure of compacted bentonite. Soils Found. 59 (1), 136–150.

Tripathy, S., Sridharan, A., Schanz, T., 2004. Swelling pressures of compacted bentonites from diffuse double layer theory. Can. Geotech. J. 41 (3), 437–450.

Villar, M.V., 2005. MX-80 bentonite. Thermo-hydro-mechanical characterisation performed at CIEMAT in the context of the Prototype project. Informes Técnicos CIEMAT 1053, Madrid.

Villar, M.V., Lloret, A., 2008. Influence of dry density and water content on the swelling of a compacted bentonite. Appl. Clay Sci. 39 (1-2), 38–49.

Yamamoto, S., Sato, S., Shimura, T., Romero, E., Nishimura, T., Owada, H., 2019. Mechanical characteristics and water retention properties of unsaturated "bentonite-based engineered barrier materials" based on controlled-suction tests. J. JSCE 75 (3), 257–272.

Ye, W.-M., Chen, Y.-G., Chen, B., Wang, Q., Wang, J.u., 2010. Advances on the knowledge of the buffer/backfill properties of heavily-compacted GMZ bentonite. Eng. Geol. 116 (1-2), 12–20.

Yong, R.N., Boonsinsuk, P., Wong, G., 1986. Formulation of backfill material for a nuclear fuel waste disposal vault. Can. Geotech. J. 23 (2), 216–228.